

Probabilistic eccentricity bifurcation for stars around shrinking massive black hole binaries

Mao Iwasa ^{*} and Naoki Seto

Department of Physics, Kyoto University, Kyoto 606-8502, Japan

Accepted XXX. Received YYY; in original form ZZZ

ABSTRACT

Based on the secular theory, we discuss the orbital evolution of stars in a nuclear star cluster to which a secondary massive black hole is infalling with vanishing eccentricity. We find that the eccentricities of the stars could show sharp transitions, depending strongly on their initial conditions. By examining the phase-space structure of an associated Hamiltonian, we show that these characteristic behaviors are partly due to a probabilistic bifurcation at a separatrix crossing, resulting from the retrograde apsidal precession by the cluster potential. We also show that separatrix crossings are closely related to realization of a large eccentricity and could be important for astrophysical phenomena such as tidal disruption events or gravitational wave emissions.

Key words: celestial mechanics, stellar dynamics – galaxies : nuclei kinematics and dynamics – Galaxy: centre

1 INTRODUCTION

The Kozai-Lidov (KL) mechanism is a well known effect for hierarchical triple systems. It oscillates the inner eccentricity and inclination, as a result of the angular momentum exchange between the inner and outer orbits. The KL mechanism was originally examined for asteroids (Kozai 1962) and satellites (Lidov 1962) by using the secular equations that is derived after averaging the mean anomalies of the two orbits. Since then, the KL mechanism has been applied to various astronomical contexts, such as evolution of triple main sequence stars (Ford, Kozinsky & Rasio 2000; Fabrycky & Tremaine 2007; Naoz & Fabrycky 2014; Borkovits et al. 2016; Toonen, Hamers & Portegies Zwart 2016), orbits of exoplanetary systems (Holman, Touma & Tremaine 1997; Ford, Kozinsky & Rasio 2000; Nagasawa, Ida & Bessho 2008; Naoz et al. 2011; Muñoz, Lai & Liu 2016), accelerated evolution of gravitational wave sources for ground based detectors (Wen 2003; Antonini & Perets 2012; Seto 2013; Antognini et al. 2014; Antonini, Murray & Mikkola 2014; Silsbee & Tremaine 2017), collisions of stars (Perets & Fabrycky 2009; Katz & Dong 2012; Thompson 2011; Kushnir et al. 2013), evolution of triple massive black hole (MBH) binaries (Blaes, Lee & Socrates 2002; Hoffman & Loeb 2007; Iwasawa et al. 2011) and so on. In addition, hierarchical four-body systems have been discussed quite recently (Pejcha et al. 2013; Hamers & Portegies Zwart 2016; Hamers & Lai 2017).

While the two original works (Kozai 1962; Lidov 1962) were made under relatively simple theoretical framework and orbital setting, advanced effects have been also studied. For example, the impacts of the outer eccentricity (Naoz 2016, see also Shappee & Thompson 2013; Michaely & Perets 2014) and the potential shortcoming of the orbital averaging scheme (Bode & Wegg 2014; Luo, Katz & Dong 2016) have been extensively discussed in the last five years. These two aspects could be important for highly eccentric inner orbits.

The KL mechanism has been examined also for nuclear star clusters (Ivanov, Polnarev & Saha 2005; Wegg & Nate Bode 2011; Chen et al. 2011; Bode & Wegg 2014; Li et al. 2014; Iwasa & Seto 2016; Stephan et al. 2016). Nowadays, almost all galaxies are considered to have MBHs in their nuclei (Ferrarese & Ford 2005). If two galaxies merge, the distance between their two central MBHs would be continuously decreased by dissipative processes, and the two MBHs are likely to coalesce in the end (Merritt 2013). Along the way, the orbits of stars in the nuclear star cluster around each MBH would be dynamically affected by the other MBH. Here, the KL mechanism could play a significant role for enhancing the tidal disruption rates or observable gravitational wave signals.

For example, Bode & Wegg (2014) examined evolution of such nuclear star clusters by numerical simulations, mainly during the stages when the distance between the two MBHs decreases relatively rapidly. Li et al. (2014) analytically studied the individual orbits of stars, by setting the distance between the two MBHs at various values (without

^{*} E-mail: iwasa@tap.scphys.kyoto-u.ac.jp

continuous variation). Iwasa & Seto (2016) analyzed how the slow and continuous contraction of the distance modifies the orbital elements of the stars. They separately included the post-Newtonian effects of the central black hole and the gravitational potential of the nuclear star cluster itself. Their analysis is based on a geometrical approach with a help of the adiabatic invariant in a time evolving phase-space (Landau & Lifshitz 1969; Murray & Dermott 2000). They reported that, when the cluster potential is included, the individual orbits of the stars could show peculiar transitions and the evolved eccentricities could have an inverted correspondence to the initial eccentricities (see Fig. 3 in Iwasa & Seto 2016).

In this paper, we continue our study on the orbital evolution of nuclear star clusters, now simultaneously including the post-Newtonian effects and the cluster potential. The resultant phase-space becomes more complicated. But, interestingly, we newly identified a probabilistic bifurcation of the inner orbital eccentricities at a separatrix crossing. Below, still using the geometrical approach, we carefully examine how this bifurcation works.

Here, we briefly mention a possible implication of this work to theoretical studies on orbital dynamics. Analyses for mean motion resonances have been one of the central topics in the field (Goldreich 1965; Sinclair 1972; Yoder 1973; Henrard & Lemaître 1983; Peale 1987; Murray & Dermott 2000; Lithwick & Wu 2012; Fabrycky et al. 2014; Goldreich & Schlichting 2014; Batygin 2015). Indeed, the simple dynamical model around the resonant capture is an impressive achievement in the theory of orbital dynamics (see *e.g.* Henrard 1982; Borderies & Goldreich 1984; Murray & Dermott 2000). Even though the phenomenon discussed in this paper are purely based on the secular theory without depending on mean anomalies, the underlying physics have similarities to the dynamics of resonant capture. In fact, our geometrical approach owes much to its successful applications to the mean motion resonances. We expect that our detailed study would inversely help us to better understand the mean motion resonances and the related theoretical techniques, from a wider point of view.

This paper is organized as follows. In §2, we describe our astronomical model and present the orbitally averaged Hamiltonian. We also discuss our system from astronomical viewpoints for nuclear star clusters, rather than the orbital dynamics. In §3, we present numerical examples to demonstrate the characteristic features at separatrix crossings. In §4, we analyze the phase-space structure, paying special attentions to the evolution of fixed points and separatrices. Then, in §5, we discuss the probabilistic bifurcation at a separatrix crossing and also analyze the large eccentricities observed during orbital evolutions. §6 is a short summary of this paper.

2 DESCRIPTION OF OUR MODEL

2.1 assumptions and settings

As shown in Fig. 1, we deal with a system composed of the following three elements: (i) the primary MBH m_0 , (ii) the associated nuclear star cluster, and (iii) the infalling secondary MBH m_2 with vanishing eccentricity. Our main interest is

the evolution of individual stars in the cluster, during the inspiral of the secondary MBH (see also Merritt 2013 for a potential role of the star clusters surrounding the perturber MBH m_2).

For simplicity, we assume that the star cluster is stationary and spherical, and has an isotropic velocity distribution. In addition, we ignore the direct gravitational interaction between stars, and only include their mutual interaction through a smooth and stationary stellar potential (see Iwasa & Seto (2016) and Appendix A for the stationarity). Then we can examine the evolution of individual stars separately, as if we merely deal with a hierarchical triple system formed by two MBHs and a single star (of course, including the cluster potential). The dynamics of the star m_1 is mainly controlled by the Newtonian potential of the primary MBH m_0 , but is perturbatively affected by its post-Newtonian effect and the gravitational potentials of the stellar cluster as well as the tertiary MBH m_2 . These three perturbative effects will appear as different terms in our secular Hamiltonian, and their competition generates interesting effects.

Here, we briefly summarize our notations. We apply the suffix j for the inner ($j=1$) and the outer ($j=2$) orbital elements. We denote the semimajor axes by a_j , the eccentricities by e_j , and the arguments of pericenters by g_j . The angle I represents the inclination between the inner and outer orbits. We also define the dimensionless inner angular momentum

$$G_1 \equiv \sqrt{1 - e_1^2}, \quad (1)$$

and its component orthogonal to the outer orbital plane

$$J_1 \equiv G_1 \cos I. \quad (2)$$

Due to the symmetry, we can fix the outer orbital plane, during its orbital decay. Meanwhile, in our analysis based on the secular theory, the inner semimajor axis a_1 as well as the projected angular momentum J_1 stay constant (as explained in §2.2). As mentioned earlier, we put $e_2 = 0$.

Next, we discuss the density profile of the spherical cluster. For the star m_1 with a fixed semimajor axis a_1 , we only need the density profile around the distance $r = a_1$ from the primary MBH. We adopt a power-law model that is parameterized as

$$\rho(r) = \rho_1 (r/a_1)^{-\beta}, \quad (3)$$

where ρ_1 is the cluster density at $r = a_1$ and the index β is in the range $0 \leq \beta < 3$ (Merritt 2013). To be concrete, we hereafter put $\beta = 3/2$, as the fiducial value.

The stellar potential causes the apsidal precession of a star in the retrograde direction, and its characteristic timescale T_{SP} (Merritt 2013) is given by

$$T_{\text{SP}} \equiv \frac{(3 - \beta)m_0}{4\pi \sqrt{1 - e_1^2} \rho_1 a_1^3} P_1 \quad (4)$$

with the inner orbital period $P_1 \approx 2\pi \sqrt{a_1^3/Gm_0}$.

The star m_1 is also affected by the first post-Newtonian (PN) effect by m_0 . It causes the apsidal precession in the prograde direction (Holman, Touma & Tremaine 1997; Ford, Kozinsky & Rasio 2000; Merritt 2013) with a characteristic timescale

$$T_{\text{1PN}} \equiv \frac{a_1^{5/2}(1 - e_1^2)}{3m_0^{3/2}}. \quad (5)$$

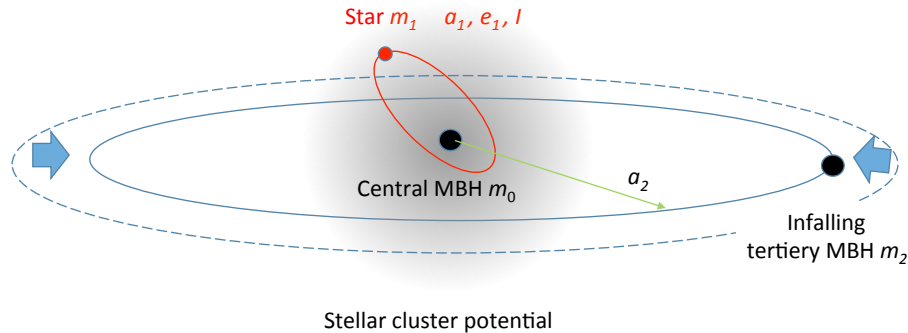


Figure 1. Configuration of our system. A star m_1 moves around the primary MBH m_0 ($\gg m_1$), perturbatively affected by (i) the 1PN effect of the primary MBH m_0 and (ii) the gravitational potential of the nuclear star cluster and (iii) the tidal field of the tertiary MBH m_2 . We denote its orbital elements by a_1 (the semimajor axis) and e_1 (the eccentricity). The secondary MBH m_2 slowly inspirals to the primary MBH with vanishing eccentricity $e_2 = 0$. The parameter I represents the inclination between the inner and outer orbits. The subscripts 1 and 2 denote the inner and outer orbital parameters.

The outer MBH has a perturbative effect on the inner orbit (for $a_1 \ll a_2$). Without the stellar potential and the 1PN correction, we can reproduce the traditional KL mechanism. More specifically, the inner eccentricity and inclination oscillate with the characteristic timescale T_{KL} (Holman, Touma & Tremaine 1997; Kinoshita & Nakai 1999; Ford, Kozinsky & Rasio 2000; Fabrycky & Tremaine 2007; Antognini 2015),

$$T_{\text{KL}} \equiv \frac{2}{3\pi} \frac{(m_0 + m_2)}{m_2} \frac{P_2^2}{P_1}. \quad (6)$$

Here, P_2 is the outer orbital period.

For the initial conditions of our system, we take a large outer distance a_2 to completely suppress the KL mechanism with $T_{\text{KL}} \gg \min[T_{\text{SP}}, T_{\text{IPN}}]$. But, along with the contraction of the outer orbit, the KL mechanism gradually becomes stronger. We will find various interesting phenomena in mid-stream.

2.2 Averaged Hamiltonian

In this paper, we focus on the long-term evolution of the inner orbit. To this end, we apply the standard secular theory to our triple systems. By the von-Zeipel canonical transformation, we can take the orbital averages with respect to the inner and outer mean anomalies (Harrington 1968; Ford, Kozinsky & Rasio 2000; Blaes, Lee & Socrates 2002). After some algebra including an appropriate scaling, we obtain the dimensionless Hamiltonian

$$\mathcal{H}_{\text{T}}(g_1, G_1) = \mathcal{H}_{\text{qp}} + \mathcal{H}_{\text{SP}} + \mathcal{H}_{\text{IPN}} \quad (7)$$

for the inner orbital elements g_1 and G_1 (composing the conjugate variables). Other dynamical variables such as the inner mean anomaly and the longitude of the inner ascending node do not appear in our Hamiltonian. Both a_1 and J_1 are conjugate to these two cyclic variables and conserved in our study.

The three terms in the Hamiltonian (7) are given by

$$\mathcal{H}_{\text{qp}} \equiv -3G_1^2 - 15\frac{J_1^2}{G_1^2} - 15(1 - G_1^2) \left(1 - \frac{J_1^2}{G_1^2}\right) \cos 2g_1, \quad (8)$$

$$\mathcal{H}_{\text{SP}} \equiv -12\eta(1 - G_1^2) \left[1 + \beta(-1 + \beta) \left(\frac{1 - G_1^2}{16} + \mathcal{O}(e_1^4)\right)\right], \quad (9)$$

$$\mathcal{H}_{\text{IPN}} \equiv \frac{24}{G_1} p\eta. \quad (10)$$

Here, J_1 is an integral of motion and β is the power-law index of the stellar cluster (see Eq. (3)). Since the parameter J_1 appears only through the form J_1^2 , we can limit $J_1 \geq 0$ without loss of generality, and the variable G_1 is bounded by $J_1 \leq G_1 \leq 1$.

In addition to the dynamical variables (g_1, G_1) , our Hamiltonian contains two important parameters η and p defined by ¹

$$\eta \equiv -\frac{4\pi\rho_1}{3m_2} a_2^3 < 0, \quad (11)$$

$$p \equiv \frac{3m_0^2}{2\pi\rho_1 a_1^4} > 0. \quad (12)$$

We will shortly explain their physical meanings.

In our Hamiltonian (7), the first term \mathcal{H}_{qp} represents the quadrupole coupling between the outer MBH and the inner orbit (Fabrycky & Tremaine 2007). We neglect the higher order couplings, because the triple system is hierarchical and the outer orbit is assumed to be circular.

In Eq. (7), the second term \mathcal{H}_{SP} originates from the Newtonian potential of the spherical stellar cluster (Merritt 2013) and is obtained by expanding a hypergeometric function with the variable $e_1 = \sqrt{1 - G_1^2}$, as in Eq. (9). With respect to this expansion, we include the higher order terms $\mathcal{O}(e_1^2)$ for our numerical calculation in §3, but we only keep the leading-order term $-12\eta(1 - G_1^2)$ for our analytical arguments in §4 and 5 (thus \mathcal{H}_{T} is independent of β). Actually, as demonstrated in §3, this truncation works quite well for physically relevant range $0 \leq \beta \leq 3$.

Our Hamiltonian depends on the outer semimajor axis a_2 through the parameter η . Note that we have $\eta \propto T_{\text{KL}}/T_{\text{SP}}$ (ignoring the e_1 -dependence). Indeed, the parameter η represents the strength of the cluster potential relative to the

¹ Our definition for η is different from Iwasa & Seto (2016) by a factor of -12 .

quadrupole coupling between the star and the outer MBH. This parameter increases with time from $\eta = -\infty$ (at $a_2 = \infty$) to $\eta = 0$ (formally at $a_2 = 0$). In our study, the parameter η works as an effective time variable showing the contraction stage of the outer orbit. Therefore, we hereafter express the total Hamiltonian (7) by $\mathcal{H}_T(g_1, G_1; \eta)$.

The last term $\mathcal{H}_{1\text{PN}}$ is the first order PN term (Blaes, Lee & Socrates 2002). In addition to η , the parameter p plays important roles in our study. We have $p \propto T_{\text{SP}}/T_{1\text{PN}}$ (again ignoring the e_1 -dependence). Therefore, this parameter shows the strength of the 1PN effect relative to the star cluster potential. As we have $a_1 = \text{const}$ in our secular analysis, it does not evolve with time ($p = \text{const}$).

The Hamiltonian approach has been a powerful method to study the dynamics of mean motion resonances (Henrard 1982; Borderies & Goldreich 1984; Murray & Dermott 2000). In that case, usually, the primary orbital parameters (*e.g.* eccentricity and inclination) are perturbatively handled with a help of disturbing function to evaluate the interaction between orbits (Murray & Dermott 2000). But, in our framework based on the expansion parameter a_1/a_2 , we can deal with a large eccentricity e_1 and a large relative inclination I . Indeed, as we see below, the maximum eccentricity corresponding to $G_1 = J_1$ plays a critical role for our phase-space evolution. This non perturbative handling of the basic orbital elements is a notable advantage of the present study.

In our preceding paper Iwasa & Seto (2016), we separately added the terms $\mathcal{H}_{1\text{PN}}$ and \mathcal{H}_{sp} to the quadrupole term \mathcal{H}_{qd} . Namely, we examined the two Hamiltonians $\mathcal{H}_{\text{qp}} + \mathcal{H}_{\text{sp}}$ and $\mathcal{H}_{\text{qp}} + \mathcal{H}_{1\text{PN}}$. But, as we see below, the competitions between the three terms enrich the phase-space structure, resulting in notable evolution of orbital elements.

2.3 Physical scales and Relaxation effects

In this paper, we basically proceed our study with the scaled Hamiltonian (7). Therefore, our main arguments are somewhat abstract. But, before going into details, in this subsection, we evaluate the actual magnitude of the dimensionless parameters p and η , using fiducial astrophysical systems. We also make a brief discussion about the relaxation effects on the inner orbit.

First, based on standard references (see *e.g.* Merritt 2013), we re-express the density profile of the nuclear star cluster as follows

$$\rho(r) = \frac{3m_0}{4\pi r_h^3} \left(\frac{r}{r_h}\right)^{-3/2}, \quad (13)$$

where r_h is the influenced radius of m_0 and is given by

$$r_h \equiv \frac{Gm_0}{\sigma^2} \quad (14)$$

with the one-dimensional velocity dispersion σ . In addition, we apply the M_\bullet - σ relation (McConnell & Ma 2013)

$$M_\bullet (= m_0) = 2.09 \times 10^8 \left(\frac{\sigma}{200\text{km/s}}\right)^{5.64} M_\odot. \quad (15)$$

Using Eqs. (13)-(15), we can fix the density profile $\rho(r)$ for a given MBH mass m_0 .

For our fiducial cluster model, the parameter p is writ-

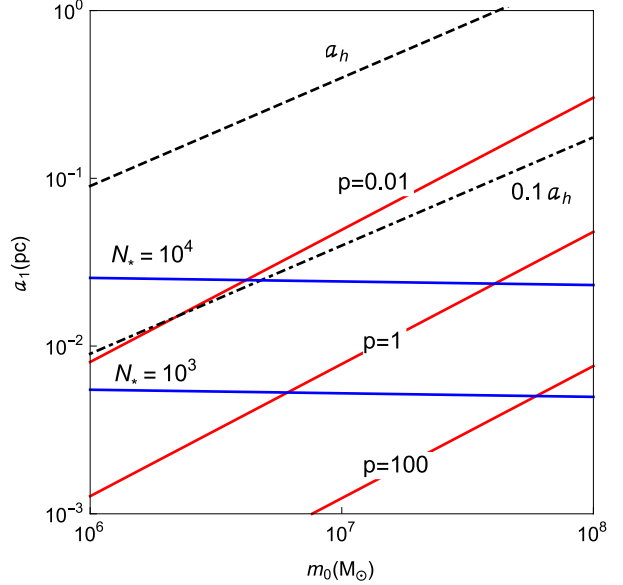


Figure 2. The contour plots for the parameter p (red lines) and the number of enclosed stars N_* (blue lines). We also show the semimajor axis a_1 in units of the hard binary separation a_h (for the mass ratio $q = 1$).

ten as

$$p = \frac{G}{c^2} \frac{3m_0^2}{2\pi\rho(a_1)a_1^4} = 5.04 \times 10^{-4} \left(\frac{a_1}{1\text{pc}}\right)^{-5/2} \left(\frac{m_0}{10^8 M_\odot}\right)^{1.97}. \quad (16)$$

In Fig.2, we present a contour plot for p .

In order to provide a rough idea about the number of stars corresponding to a given parameter p , we define the integral

$$N_*(< a_1) = \frac{1}{m_*} \int_0^{a_1} 4\pi r^2 \rho(r) dr, \quad (17)$$

which approximately represents the total number of stars with semimajor axis less than a_1 . Here, m_* is the typical mass of stars in the cluster. In Fig.2, we show the enclosed numbers $N_*(< a_1)$, by setting $m_* = 1M_\odot$.

Meanwhile, the parameter η depends also on the outer semimajor axis a_2 . In order to specify its typical range relevant for our study, we briefly introduce the standard arguments on the orbital decay of a MBH binary (Merritt 2013).

After the merger of two galaxies, the distance between their central MBHs decreases due to dynamical friction and sling-shot ejections of stars. But, when the binary separation decreases down to the so-called hard binary separation

$$\begin{aligned} a_h &\equiv \frac{m_2}{m_0 + m_2} \frac{r_h}{4} \\ &= 3.51 \frac{q}{q+1} \left(\frac{m_0}{10^8 M_\odot}\right)^{0.645} \text{pc}, \end{aligned} \quad (18)$$

($q \equiv m_2/m_0$), the infall time is considered to increase significantly, though its actual value is highly uncertain (also depending strongly on the environment around the binary).

In our theoretical framework based on the adiabatic invariant (explained in §5), the slow contraction of the outer orbits is essential. Therefore, below, we consider the range $a_2 \lesssim a_h$ for the outer orbit.

Once the outer distance a_2 is given, the dynamical stability of the triple system imposes the hierarchical orbital configuration $a_1 \lesssim 0.1a_2$ for the inner orbit, assuming comparable MBH masses $q = m_2/m_0 \sim 1$ (Mardling & Aarseth 2001). Therefore, in Fig.2, our target star should have semi-major axis $a_1 \lesssim 0.1a_h$.

Next, we examine the parameter η . It is written in terms of a_2 and a_1/a_2 as

$$\begin{aligned} \eta &= -\frac{m_0}{m_2} \left(\frac{a_2}{r_h}\right)^{3/2} \left(\frac{a_1}{a_2}\right)^{-3/2} \\ &= -44.3 \left(\frac{F(q)}{F(1)}\right) \left(\frac{a_2}{a_h}\right)^{3/2} \left(\frac{a_1/a_2}{0.01}\right)^{-3/2}, \end{aligned} \quad (19)$$

with $F(q) \equiv \sqrt{q/(1+q)^3}$. We should recall that the inner semimajor axis a_1 stays constant in our secular analysis. With this expression, we can read how the parameter $\eta (< 0)$ increases (from a large negative value), along with the contraction of the outer radius a_2 .

Finally, we comment on the relaxation processes that will not be handled in our main arguments. Here, following our previous paper (Iwasa & Seto 2016), we concentrate on the resonant relaxation. This is because, in the nuclear star clusters, the timescale of resonant relaxation is generally much smaller than that of the two-body relaxation.

The resonant relaxation is a diffusion process in the angular momentum space (Rauch & Tremaine 1996; Alexander 2005; Kocsis & Tremaine 2011). It is classified into two categories; the scalar and vector types. While the scalar resonant relaxation changes both the magnitude and orientation of the angular momentum, the vector resonant relaxation changes only the orientation of the angular momentum.

In our previous paper (Iwasa & Seto 2016), we examined the impact of the outer MBH on these two types. We showed that the vector type is not effective around the evolutionary phase in interest (*e.g.* at the separatrix crossing) due to the overall precession around the symmetry axis normal to the outer orbital plane. In contrast, the scalar resonant relaxation could become effective, if its characteristic timescale $T_{\text{rr,s}}$ is smaller than the infall time $T_{\text{inf}} = |a_2/\dot{a}_2|$. When the inner apsidal precession is dominated by the cluster potential, the timescale $T_{\text{rr,s}}$ is explicitly given by

$$\begin{aligned} T_{\text{rr,s}} &= \frac{m_0}{m_1} P_1 \\ &= 1.6 \times 10^9 \left(\frac{1M_\odot}{m_1}\right) \left(\frac{m_0}{10^8 M_\odot}\right)^{1/2} \left(\frac{a_1}{0.3\text{pc}}\right)^{3/2} \text{ yr}. \end{aligned} \quad (20)$$

We can ignore the resonant relaxation, if the infall time satisfies the following condition

$$T_{\text{inf}} < T_{\text{rr,s}}. \quad (21)$$

3 NUMERICAL EXAMPLES

In this paper, our primary objective is to analytically examine the Hamiltonian (7) and related dynamics. But, numerical demonstrations would be also helpful to provide intuitive pictures of our targets. In this section, we first show results for the two numerical runs R1 and R2 that have nearly iden-

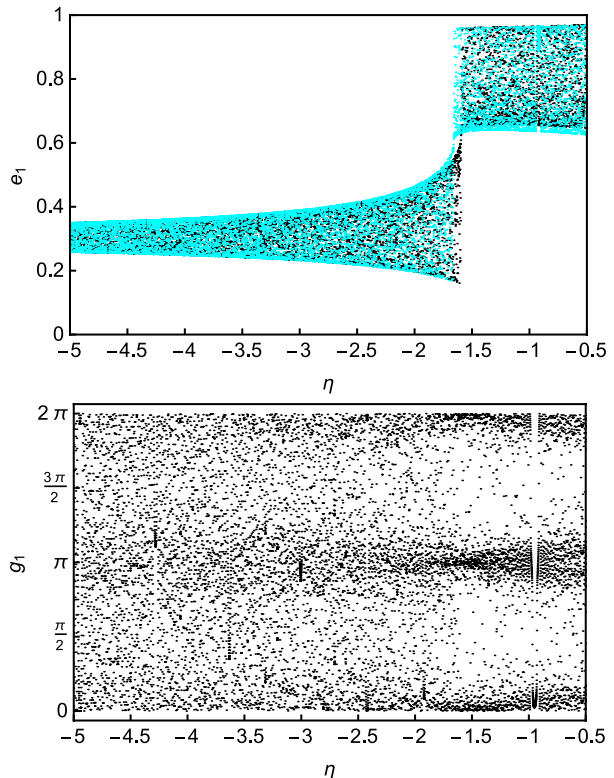


Figure 3. (Black points) Numerical results for the run R1, including the higher order terms for \mathcal{H}_{SP} in Eq. (9) with $\beta = 1.5$. The initial condition is $(g_1, G_1) = (0.03, 0.950)$ at $\eta = -20$ with the time-independent parameters $(J_1, p) = (0.2, 0.2)$. We show the inner eccentricity e_1 and the argument of pericenter g_1 as a function of the effective time η . We can observe the single transition at $\eta \approx -1.65$. The short-term vertical patterns (*e.g.* around $\eta = -3.60$) are artificially caused by our data sampling scheme. (Cyan points) Numerical results for the run R3, only with the lowest order terms for \mathcal{H}_{SP} (corresponding to $\beta = 1$). The initial condition is $(g_1, G_1) = (0.04, 0.950)$ at $\eta = -20$.

tical initial conditions but later evolve in entirely different ways.

The two runs have the same time-independent parameters $(p, J_1) = (0.2, 0.2)$. At the effective time $\eta = -20$, we set their initial conditions $(g_1, G_1) = (0.03, 0.950)$ for R1 and $(0, 0.950)$ for R2. Thus, only the initial phases g_1 are slightly different.

For the two runs R1 and R2, we included the higher order corrections for the terms \mathcal{H}_{SP} in Eq. (9), and numerically integrated the canonical equations

$$\frac{dg_1}{dt} = \frac{\partial \mathcal{H}_T}{\partial G_1}, \quad \frac{dG_1}{dt} = -\frac{\partial \mathcal{H}_T}{\partial g_1} \quad (22)$$

with setting the outer decay rate at $d\eta/dt = 0.01$. Note that, with our scaled Hamiltonian (7), the circulation/libration period of the angle g_1 is typically $\mathcal{O}(1)$ and much smaller than the variation timescale $\eta/\dot{\eta}$ of the parameter η .

In Figs. 3 and 4, with the black points, we show the evolution of the inner orbital elements e_1 and g_1 for the two runs R1 and R2, as a function of the effective time η . We only plot the range $\eta > -5$, since the two system evolved almost identically in the earlier stage. In Fig. 3, the eccentricity

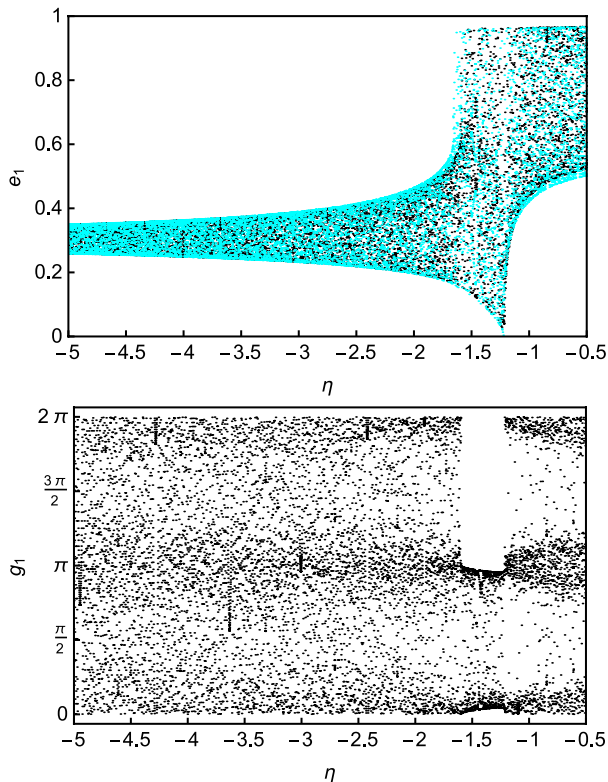


Figure 4. (Black points) Numerical results for the run R2, including the higher order terms for \mathcal{H}_{SP} . The initial condition $(g_1, G_1) = (0, 0.950)$ is slightly different from R1 (shown in Fig. 3). We have two transitions at $\eta \approx -1.65$ and -1.20 . Between them, the angle g_1 librates around $\pi/2$. (Cyan Points) Numerical results for the run R4, only with the lowest order terms for \mathcal{H}_{SP} . The initial condition is $(g_1, G_1) = (0.01, 0.950)$.

e_1 shows a sharp transition around $\eta = -1.65$. Its oscillation range discontinuously shifted from $(0.18, 0.60)$ to $(0.60, 0.96)$.

However, in Fig. 4, around the same epoch $\eta = -1.65$, the eccentricity e_1 turned into a wider amplitude oscillation from the original range $(0.18, 0.60)$ to the new one $(0.18, 0.96)$. At the same time, the angle g_1 was captured into a libration around $g_1 = \pi/2$. This libration state terminated around $\eta = -1.20$, and, we concurrently had $e_1 \approx 0$. Therefore, in distinction from Fig. 3, Fig. 4 has two clear transitions, even though these two runs have almost the same initial conditions.

In Figs. 3 and 4, using the cyan points, we show the numerical results for two additional runs R3 (Fig. 3) and R4 (Fig. 4), now only keeping the lowest order term for \mathcal{H}_{SP} (corresponding to $\beta = 1$). Their initial phases are $g_1 = 0.04$ (R3) and 0.01 (R4) that are not identical to R1 and R2, reflecting the probabilistic nature of the bifurcation, as explained later. In Figs. 3 and 4, the two runs R3 and R4 reproduce the characteristic features of the original runs R1 and R2 quite well, with small shifts of the characteristic epochs. We additionally examined the cases with $\beta = 0.5$ and 1.75 (the Bahcall-Wolf profile), and confirmed their time profiles are also similar to the cyan points in Figs. 3 and 4. More quantitatively, for example, the first transition epochs η (as seen in Fig.3) for the four slopes β are -1.68 ($\beta = 0.5$), -1.66 (1.0), -1.65 (1.5) and -1.55 (1.75). Indeed, the shifts

Table 1. Definitions of symbols in our phase space

Legend	definition
filled circle	stable fixed point
open circle	unstable fixed point
for the fixed points at $G_1 = J_1$ and 1	
thick solid line	stable fixed point
dashed line	unstable fixed point
dotted line	marginality stable fixed point
thin black line	contour of Hamiltonian
red line	upper separatrix
blue line	lower separatrix

are small for the realistic range of β , supporting the validity of our truncation.

Therefore, below, we only keep the lowest order term for \mathcal{H}_{SP} . This considerably simplifies our Hamiltonian, and allows us to develop analytical evaluations.

As demonstrated in Figs. 3 and 4, the evolution of a system could depend strongly on its initial condition. In the following sections, we show that these interesting results are due to the probabilistic bifurcation at a separatrix crossing. The orbital evolution at a separatrix crossing is one of the central issues in this paper.

4 STRUCTURE OF PHASE SPACE

Next, we analytically explain the evolution of the phase space structure for the Hamiltonian (7) that depends on the effective time variable η . As we see in §4.2, the separatrices determine the basic profile of the phase space, dividing the librating and circulating regions.

Meanwhile, a separatrix starts from and runs into unstable fixed points. Therefore, to follow the evolutions of the separatrices, it is crucial to understand the transitions of the fixed points, in response to our time variable η . This preparative study is done in §4.1.

In the following, we limit the angular variable g_1 in the range $[0, \pi)$, identifying $g_1 = \pi$ with $g_1 = 0$, because of the symmetry of the Hamiltonian (7).

4.1 Transitions of the fixed points

In this section, we identify the five types of transitions T1-T5 when the basic properties of the fixed points (*e.g.* their total number, stabilities) change in our phase space. As we explain below, these transitions are accompanied by merger or split of multiple fixed points, and classified as the pitchfork bifurcation in the literature (*e.g.* Strogatz 2014).

To begin with, we should point out that, in the (g_1, G_1) coordinate, the inner argument of pericenter g_1 becomes singular at $G_1 = J_1$ and 1. This is because the angle g_1 loses its geometrical meanings there. More specifically, the inner orbit is circular for $G_1 = 1$ and is coplanar with the outer orbit for $G_1 = J_1$ (namely $\cos I = 1$), both making the angle g_1 ill-defined. But, we can overcome these coordinate singularities at $G_1 = J_1$ and 1, by applying the following canonical trans-

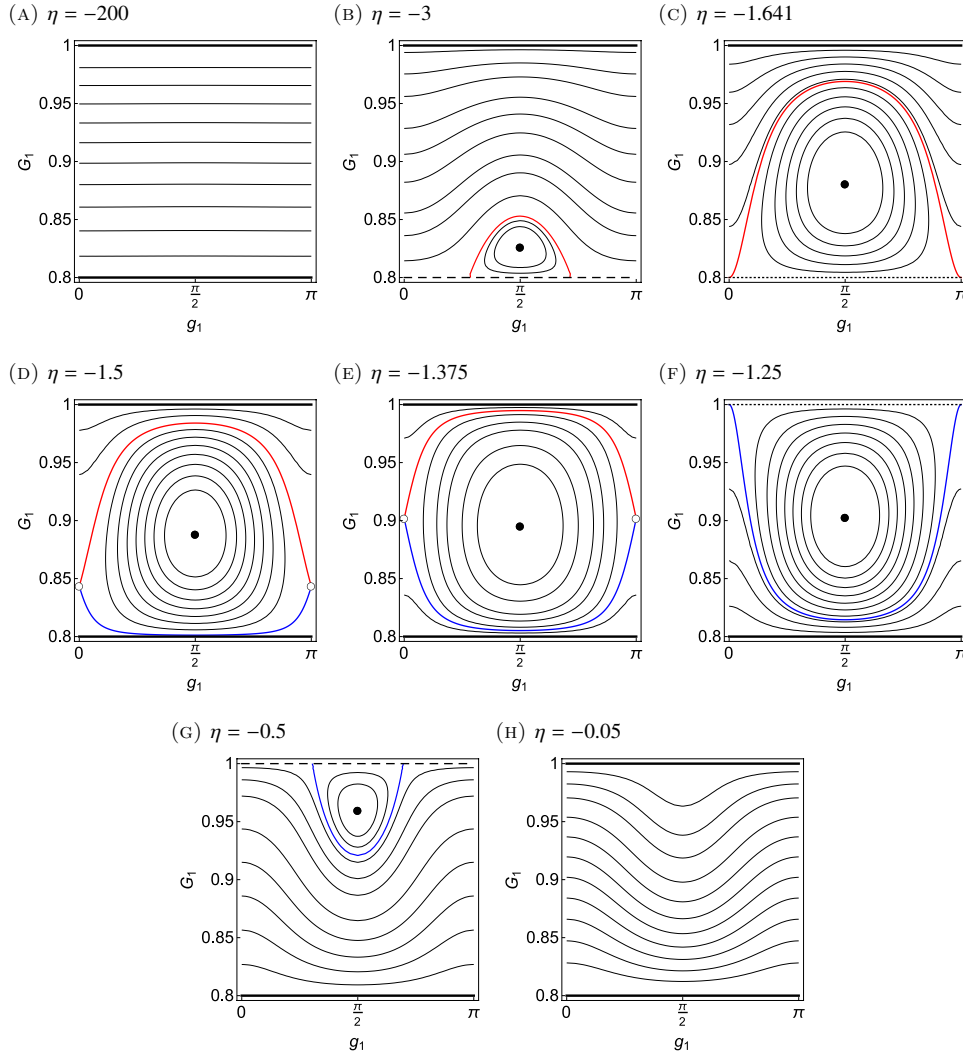


Figure 5. Evolution of the phase space for $(J_1, p) = (0.8, 0.2)$. We present the snapshots from $\eta = -200$ to -0.05 . The thin black lines are contours of Hamiltonian (7). The red and blue lines represent separatrices. The black dots and open circles are stable and unstable fixed points respectively. At the upper and lower boundaries $G_1 = 1$ and $G_1 = J_1$, the angular variable g_1 has coordinate singularities and these two boundaries should be regarded as two points (though artificially represented as lines). They are actually fixed points, and we show their stabilities by using different types of lines; stable (thick solid lines), unstable (dotted lines) and marginally stable (dashed lines). The legends are summarized in Table 1.

formations respectively (Ivanov, Polnarev & Saha 2005);

$$(x', y') = \sqrt{2(G_1 - J_1)}(\sin g_1, \cos g_1), \quad (23)$$

$$(x, y) = \sqrt{2(1 - G_1)}(\cos g_1, \sin g_1). \quad (24)$$

In these regular coordinates (x', y') or (x, y) , we can readily find that the points $(x', y') = (0, 0)$ and $(x, y) = (0, 0)$ (thus $G_1 = J_1$ and 1) are always fixed points.

Below, we continue to use the original coordinate (g_1, G_1) in which the two fixed points $G_1 = J_1$ and 1 are stretched into two horizontal lines (as demonstrated below in Fig. 5). We distinguish their stabilities by using the following three types of lines; thick solid lines (stable), dotted lines (unstable) and dashed lines (marginally stable).

For the standard KL mechanism (i.e. $\eta = 0$ for Eq. (7)), the fixed point $G_1 = J_1$ is always stable, and the stability of another fixed point $G_1 = 1$ is solely determined by J_1

($J_1 > \sqrt{3/5}$: stable, $J_1 < \sqrt{3/5}$: unstable, Kozai 1962; Lidov 1962). By stark contrast, in our study, both of the fixed points $G_1 = J_1$ and 1 change their stabilities, depending on p, η and J_1 , as we see below.

In Fig. 5, for $(J_1, p) = (0.8, 0.2)$, we show the evolution of contours of the Hamiltonian (7) in the phase space (g_1, G_1) . We show the stable and unstable fixed points with the black dots and the open circles respectively (in addition to the lines for the two fixed points $G_1 = J_1$ and 1 mentioned above). As discussed in the next subsection, the separatrices can be divided into the upper and lower parts. They are shown with the red and blue lines whose definitions are given in the next subsection. We summarized the legends of our phase-space figures in Table 1.

In Fig. 5, as η increases due to the outer orbital decay, we can see the following four transitions T1, T2, T3 and

Table 2. The five transitions when the fixed points change their basic properties. Column 2; the point where an additional fixed point is created or annihilated. The g_1 coordinate is the asymptotic value. Columns 3 and 4; the stabilities of fixed points $G_1 = J_1$ and 1 around the transition (S: stable, U: unstable). Column 5; the effective time parameter η_i at each transition T_i . Column 6; the parameter region (J_1, p) to realize the valid sign $\eta_i < 0$.

	fixed point creation/annihilation	Stability of $G_1 = J_1$	Stability of $G_1 = 1$	epoch η	corresponding region
T1	creation at $(g_1, G_1) = (\pi/2, J_1)$	S \rightarrow U	S	$\eta_1 = -\frac{-3J_1^3 + 5J_1}{2(J_1^3 - p)}$	$p < J_1^3$
T2	creation at $(0, J_1)$	U \rightarrow S	S	$\eta_2 = -\frac{J_1^3}{J_1^3 - p}$	$p < J_1^3$
T3	annihilation at $(0, 1)$	S	S \rightarrow U	$\eta_3 = -\frac{1}{1-p}$	$p < 1$
T4	annihilation at $(\pi/2, 1)$	S	U \rightarrow S	$\eta_4 = -\frac{-3+5J_1^2}{2(1-p)}$	$p < 1$ and $J_1 > \sqrt{3/5}$
T5	creation at $(\pi/2, 1)$	S	S \rightarrow U	$\eta_5 = -\frac{-3+5J_1^2}{2(1-p)}$	$p > 1$ and $J_1 < \sqrt{3/5}$

T4, when the fixed points change their basic properties. We explain them one by one, using Fig. 5.

T1: This transition occurs between Figs. 5a and 5b. The new fixed point (shown by the black dots in Fig. 5) appears at $G_1 = J_1$, and starts moving upward along the line $g_1 = \pi/2$. The stability of the fixed point $G_1 = J_1$ (shown by lines) turns from stable to unstable.

T2: This transition occurs at Fig. 5c. The new fixed point appears at $G_1 = J_1$, and starts moving upward along the line $g_1 = 0$ (shown as the open circles in Fig. 5). The stability of the fixed point $G_1 = J_1$ turns from unstable to stable.

T3: This transition is at Fig. 5f. The fixed point on $g_1 = 0$ (created at T2) disappears at $G_1 = 1$. The stability of the fixed point $G_1 = 1$ turns from stable to unstable.

T4: This transition is between Figs. 5g and 5h. The fixed point on $g_1 = \pi/2$ (created at T1) disappears at $G_1 = 1$. The stability of the fixed point $G_1 = 1$ turns from unstable to stable.

We summarize the primary aspects of these four transitions T1, T2, T3 and T4 in Table 2. Here, it is important to notice that these transitions always accompany the creations (at $G_1 = J_1$) or annihilations (at $G_1 = 1$) of the fixed point that moves upward either along $g_1 = 0$ or $\pi/2$. Concurrently, the corresponding fixed point $G_1 = J_1$ or 1 also changes its stability. These transitions are typical pitchfork bifurcations (Strogatz 2014).

Now we explicitly evaluate the effective time parameter η_1 for the transition T1. Firstly, for the stable fixed point shown with the black dots in Fig. 5 at $g_1 = \pi/2$, we derive the relation between the coordinate value G_1 and the time parameter η . Then we specify the transition epoch η_1 , using the condition that, at T1, this fixed point takes the coordinate value $G_1 = J_1$ (see Table 1).

Since we identically have $\partial\mathcal{H}_T/\partial g_1 = 0$ for $g_1 = \pi/2$, the desired relation between G_1 and η is given as $\partial\mathcal{H}_{T,1}/\partial G_1|_{g_1=\pi/2} = 0$, or

$$-3G_1 + 5\frac{J_1^2}{G_1^3} = -2\eta\left(G_1 - \frac{p}{G_1^2}\right). \quad (25)$$

Plugging-in $G_1 = J_1$, we obtain the transition epoch for T1

$$\eta_1 \equiv -\frac{-3J_1^3 + 5J_1}{2(J_1^3 - p)}. \quad (26)$$

Considering the inequalities $0 \leq J_1 \leq 1$, this solution has

the appropriate sign $\eta_1 < 0$ only for $p < J_1^3$. We present these results in the fifth and sixth columns in Table 2.

Similarly, we can derive η_2 for T2. For the unstable fixed point at $g_1 = 0$ (shown with the open circles in Fig. 5), we identically have $\partial\mathcal{H}_T/\partial g_1 = 0$ again, and the relation between G_1 and η is now given as

$$G_1 = -\eta\left(G_1 - \frac{p}{G_1^2}\right). \quad (27)$$

Putting $G_1 = J_1$ for the transition T2, we have

$$\eta_2 \equiv -\frac{J_1^3}{J_1^3 - p} \quad (28)$$

which has the valid sign $\eta_2 < 0$ for $p < J_1^3$. For $(J_1, p) = (0.8, 0.2)$, we indeed have $\eta_2 = -1.641$ consistent with Fig. 5c.

We can also derive η_4 and η_3 by setting $G_1 = 1$ in Eqs. (25) and (27) respectively. The results for T2, T3 and T4 are summarized in Table 2. We should notice the chronological order of the transitions $\eta_1 < \eta_2 < \eta_3 < \eta_4 < 0$ in the parameter region (J_1, p) simultaneously satisfying the inequalities for T1 to T4 listed in Table 1.

So far, we have discussed the four transitions T1, T2, T3 and T4 that are realized for $(J_1, p) = (0.8, 0.2)$ when increasing η from $-\infty$ to 0. However, these are not the complete set of the transitions observed for the valid parameter range $0 \leq p$ and $0 \leq J_1 \leq 1$. In fact, we have an additional transition T5, as demonstrated in Fig. 6 for $(J_1, p) = (0.5, 1.2)$. The basic aspects of T5 is summarized in Table 1. This is almost the inverse of the transition T4, and appears only for $p > 1$ and $J_1 < \sqrt{3/5}$. We have the transition epoch η_5 whose expression is identical to η_4 (as easily understood from their derivations). The newly generated stable fixed point (shown with the black dots in Fig. 6) moves downward, as η increases from η_5 .

Given the inequalities in the last column in Table 1, we can divide the parameter space (J_1, p) into the six different regions I to VI, as shown in Fig. 7. The transitions observed in each region are summarized in Table 3.

For simplicity, we have not discussed the situations just on the boundaries of these six regions. But, at this stage, it would be instructive to comment on our previous work (Iwasa & Seto 2016) where we simply put $p = 0$ (ignoring relativistic corrections) to examine the effects of the stellar potential. For $p = 0$, the two transitions T2 and T3 are degenerated at the epoch $\eta_2 = \eta_3 = -1$ where the phase space goes through a drastic transition (see Fig. 3c in Iwasa & Seto

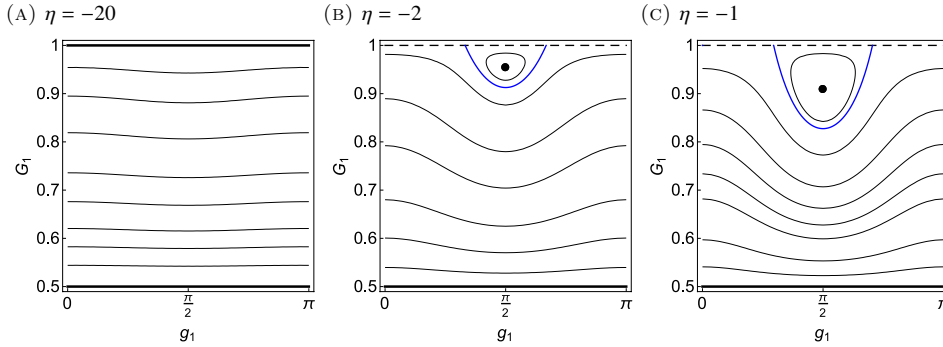


Figure 6. Evolution of the phase space for the region V with $(J_1, p) = (0.5, 1.2)$. We show the snapshots at $\eta = -20, -2, \text{ and } -1$.

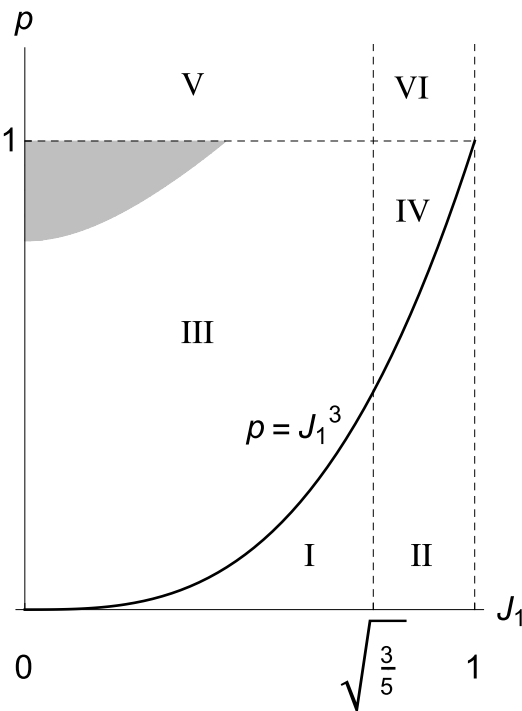


Figure 7. The classification of the parameter space (J_1, p) , according to the realized transitions T1 to T5 (see Table 2). In the shaded area in III the probabilistic bifurcation does not occur (explained in §5.4).

Table 3. The transitions realized in the regions I - VI

Region	Transitions
I	T1, T2, T3
II	T1, T2, T3, T4
III	T3
IV	T3, T4
V	T5
VI	none

2016).² In contrast, with a finite p , we have $\eta_2 \neq \eta_3$ for $J_1 < 1$, and the anomalous behaviors for $p = 0$ are “regularized” as demonstrated in Fig. 5.

4.2 Evolution of the phase-space structure

In the previous subsection, we analyzed the transitions T1 to T5 realized at the specific epochs η_i ($i = 1, \dots, 5$). Now, we discuss the evolution of the phase-space structure for more general values of $\eta \neq \eta_i$. We pay special attention to the separatrices that play central roles here, dividing the librating and circulating regions.

For a one dimensional Hamiltonian system, an unstable fixed point is generally categorized as a saddle, while a stable one as a center (Strogatz 2014). This is because the Hesse matrix for the stability analysis is traceless, due to the canonical equations of motion. But, for simplicity, we merely call them unstable and stable fixed points.

In our phase space, the separatrices begin and end at unstable fixed points, as already demonstrated in Fig. 5. Therefore, for our Hamiltonian, the basic structure of the separatrices can change only at the five transitions T1 - T5 listed in Table 2. Strictly speaking, just at these transitions (see *e.g.* Fig. 5f for T4), the relevant fixed point becomes marginally stable, namely, an intermediate state between stable and unstable.

To begin with, we examine a concrete example. In Fig. 7, the point $(J_1, p) = (0.8, 0.2)$ belongs to the region II which has the four transitions T1 to T4 as shown in Table 2. Therefore, when increasing η from $-\infty$ to 0, its phase space can take the five patterns P0 to P4, divided by the four transitions as follows

$$P0 \rightarrow T1 \rightarrow P1 \rightarrow T2 \rightarrow P2 \rightarrow T3 \rightarrow P3 \rightarrow T4 \rightarrow P4.$$

In Fig. 8, we provide the examples of the five patterns P0 to P4 that individually have distinct topological profiles with respect to the separatrices and the fixed points. Actually, as we see later, these five patterns are the complete set (except for the phase spaces just at the transitions T_i) for the

² For $p = 0$ and $\eta = -1$, every point on the line $g_1 = 0$ satisfies $\partial\mathcal{H}_{T,1}/\partial G_1 = \partial\mathcal{H}_{T,1}/\partial g_1 = 0$ and can be regarded as a fixed point. But, for $\eta \neq -1$, we do not have an unstable fixed point at $g_1 = 0$ that is crucially important for the probabilistic bifurcation discussed later.

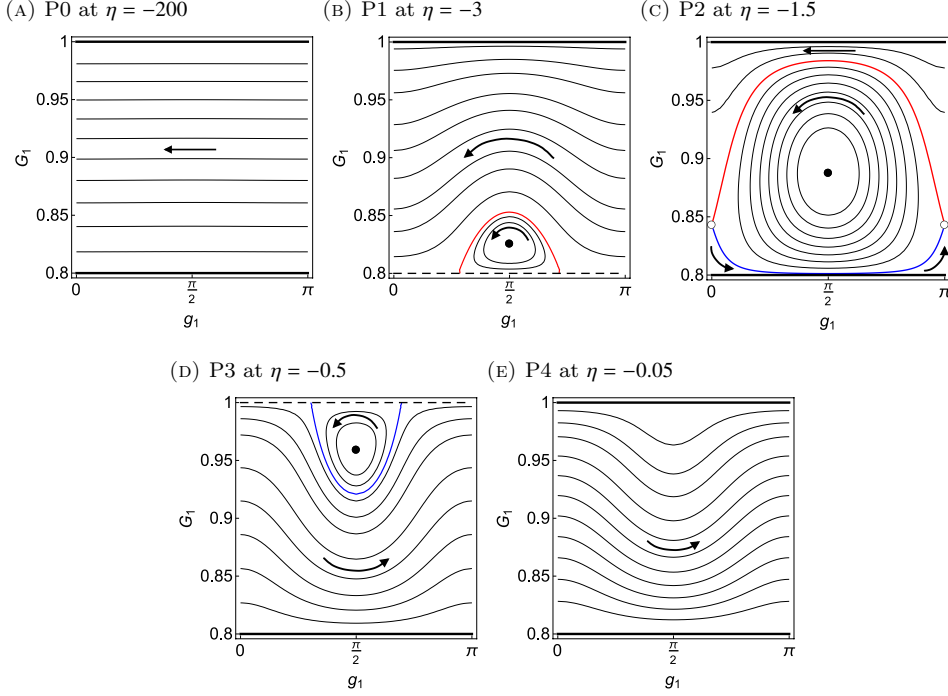


Figure 8. Phase-space evolution for the region II with $(J_1, p) = (0.8, 0.2)$ (same as Fig. 5) that has the four transitions T1 ($\eta_1 = -3.94$), T2 ($\eta_2 = -1.64$), T3 ($\eta_3 = -1.25$) and T4 ($\eta_4 = -0.125$). We present the five distinct phase-space patterns P0, P1, P2, P3 and P4 separated by the four transitions. The separatrices begin and end at the corresponding unstable fixed points. The red curves are the upper separatrix $\tilde{G}_{1,+}(g_1, \eta)$, while the blue curves are the lower ones $\tilde{G}_{1,-}(g_1, \eta)$. The arrows represent the direction of trajectories. In panel c, the lower circulating region (below the blue curve) becomes narrow around $g_1 = \pi/2$, but the blue curve does not touch the fixed point $G_1 = J_1$ shown with the thick solid line.

whole regions in Fig. 7, including the region V that has the transition T5 different from T1 to T4 (see Table 2).

In Fig. 8, the separatrices are presented with the red and blue curves. In this paper, we define $G_1 = \tilde{G}_{1,+}(g, \eta)$ for the upper separatrix curve above the associated unstable fixed point,³ and represent it with a red curve. Here $\tilde{G}_{1,+}(g, \eta)$ should be regarded as a function of g_1 and η (omitting the dependence on the constant parameters p and J_1). Similarly, we define $G_1 = \tilde{G}_{1,-}(g, \eta)$ for the lower separatrix curve below the associated unstable fixed point, showing it with a blue curve.

In Fig. 8b, the pattern P1 has only the upper separatrix curve $G_1 = \tilde{G}_{1,+}(g_1, \eta)$. Since it passes through the unstable fixed point $G_1 = J_1$ and satisfies $\mathcal{H}_T = \text{const}$, the function $\tilde{G}_{1,+}(g_1, \eta)$ is algebraically obtained by solving the following quartic equation for the total Hamiltonian $\mathcal{H}_T(g_1, G_1; \eta)$ defined in Eq.(7)

$$\mathcal{H}_T(\cdots, J_1; \eta) = \mathcal{H}_T(g_1, \tilde{G}_{1,+}(g_1, \eta); \eta), \quad (29)$$

where, in the left-hand side, we explicitly show that our Hamiltonian does not depend on g_1 at $G_1 = J_1$.

Meanwhile, the pattern P2 in Fig. 8c has both the upper and lower separatrices associated with the unstable point at $g_1 = 0$. We can obtain the G_1 -coordinate of the fixed point

$G_1^*(\eta)$ from the cubic equation given in Eq.(27)

$$G_1^*(\eta) = -\eta \left(G_1^*(\eta) - \frac{p}{G_1^*(\eta)^2} \right) \quad (30)$$

which has a valid solution for $\eta_2 < \eta < \eta_3$, as explained in the previous subsection. Then, similar to Eq.(29), we can derive the upper $\tilde{G}_{1,+}(g_1, \eta)$ and lower $\tilde{G}_{1,-}(g_1, \eta)$ separatrix curves as the two appropriate solutions for the quartic equation

$$\mathcal{H}_T(0, G_1^*(\eta); \eta) = \mathcal{H}_T(g_1, \tilde{G}_{1,\pm}(g_1, \eta); \eta). \quad (31)$$

For the pattern P3 shown in Fig. 8d, we can derive the expression for the lower separatrix $G_1 = \tilde{G}_{1,-}(g_1, \eta)$ by using

$$\mathcal{H}_T(\cdots, 1; \eta) = \mathcal{H}_T(g_1, \tilde{G}_{1,-}(g_1, \eta); \eta), \quad (32)$$

as in the case for the pattern P1 (see Eq.(29)).

Now we briefly discuss the phase-space structure for the patterns P0 to P4. In Fig. 8, a librating region exists for the patterns P1, P2 and P3, and the orientation of the libration is counter-clockwise. Meanwhile, the region above the upper separatrix (red curve) is always circulating in the retrograde direction, dominated by the stellar potential. This is also true for the whole region of P0, as easily expected from the continuity of the system (see Figs. 8a and 8b). In contrast, the region below the lower separatrix (and also the whole region of P4) has prograde circulation. Here, the quadrupole or 1PN effect dominates the apsidal precession.

In Fig. 8, only the pattern P2 simultaneously has the three types of motions, divided by the two separatrices. This phase space structure is similar to that of a simple pendu-

³ More precisely, the value of the G_1 coordinate is larger than that of the associated unstable fixed point.

lum whose Hamiltonian is given by $(P^2 + \sin 2Q)/2$ for the conjugate variables (Q, P) (but without the two fixed points corresponding to $G_1 = J_1$ and 1 for our Hamiltonian).

So far, we have studied the evolution of the phase-space structures specifically for the region II in Fig. 7. Below, we discuss other regions. As shown in Table 3, the transitions of the regions I, III, and IV are subsets of those for the region II.

For example, the region II has the single transition T3 and, therefore, its evolutionary sequence is given as

$$P2 \rightarrow T3 \rightarrow P3.$$

To demonstrate this explicitly, in Fig. 9, we present the snapshots for $(J_1, p) = (0.2, 0.2)$ for which we have the transition epoch $\eta_3 = -1.25$. Note that, when decreasing η down toward $-\infty$, the area of the libration region approaches to 0, and the red and blue curves become more symmetric with respect to the stable fix point shown with the filled circle. The G_1 coordinate of the fixed point approaches $p^{1/3}$.

In the same manner, for the region I, we have the time sequence

$$P0 \rightarrow T1 \rightarrow P1 \rightarrow T2 \rightarrow P2 \rightarrow T3 \rightarrow P3,$$

and

$$P2 \rightarrow T3 \rightarrow P3 \rightarrow T4 \rightarrow P4$$

for the region IV.

On the other hand, the region V has the single transition T5 that is essentially an inverse of T4 (see Table 2), and we have the sequence

$$P4 \rightarrow T5 \rightarrow P3.$$

Finally, the region VI has no transition and its phase space always corresponds to the pattern P4.

When we drop the stellar potential term \mathcal{H}_{SP} with $\rho_1 = 0$, the combination $\eta' \equiv \eta p \leq 0$ now becomes the appropriate parameter to characterize the contraction of the outer orbit (see §2.2). We can easily confirm that, in this case, only the two patterns P3 and P4 are realized, as for the standard KL-mechanism. As we see later, the patterns P1 and P2 cause interesting effects for the inner orbit, but these appear only with the stellar potential term \mathcal{H}_{SP} .

5 BIFURCATION AT SEPARATRIX CROSSING

In the previous section, we discussed how the phase-space structure evolves along with the contraction of the outer orbit. We paid special attention to the profiles of the separatrices. In this section, we study the evolution of individual trajectories in the time-varying phase space, such as Figs. 8 and 9. In §5.1, we introduce the idea of the adiabatic invariant and then, in §5.2, apply it to the numerical demonstrations in Figs. 3 and 4. In §5.3, we make somewhat formal arguments on the probabilistic bifurcations at the separatrix crossings for the pattern P2. In §5.4, we discuss the probabilistic bifurcations for our hierarchical triple systems. In §5.5, for individual orbits, we examine the maximum eccentricities observed in a certain time interval.

5.1 adiabatic invariant

Firstly, we explain the adiabatic invariant for a one-dimensional Hamiltonian $\mathcal{H}(q, p; \lambda)$ that contains a time-varying parameter λ . In the phase space (q, p) , we consider the time evolution of a periodic trajectory described by this Hamiltonian. If the timescale of the variation of λ is much larger than the rotation period of the trajectory, the following integral is conserved

$$S(\lambda) \equiv \oint p(q, \lambda) dq, \quad (33)$$

and known as an adiabatic invariant (Landau & Lifshitz 1969; Peale 1987; Murray & Dermott 2000). Here the integral is taken for the trajectory that can be effectively regarded as periodic. In the phase space, this integral corresponds to the area inside the periodic trajectory. This geometrical interpretation allows us to intuitively follow the time evolution of a trajectory in the phase space. We just need to track contours whose relevant areas are the same.

For our Hamiltonian (7), the characteristic time-scale of the orbit is $O(1)$, and thus we should have $|\eta/(d\eta/dt)| \gg 1$ for applying the adiabatic invariant.

Here, we should comment on a technical detail about the definition of the adiabatic invariants for circulating trajectories. In Fig. 8, unlike a librating trajectory, a circulating trajectory is not literary periodic in the (g_1, G_1) coordinate. But, it becomes periodic with the regular coordinate (x', y') defined in Eq. (23), and the adiabatic invariant can be straightforwardly defined. Inversely, in the original coordinate (g_1, G_1) , this adiabatic invariant for a circulating trajectory corresponds to the area between the line $G_1 = J_1$ and the trajectory, and we employ this geometrical interpretation below. Note also that the area for a librating trajectory is identical in both coordinates, as they are related by a canonical transformation. Here, we implicitly assume to appropriately handle the contracted range for the angular variable g_1 ($[0, 2\pi)$ to $[0, \pi)$ as explained in §4).

For using the adiabatic invariant, we need a careful analysis when a trajectory crosses a separatrix. A separatrix crossing is a quite interesting phenomenon and is the underlying mechanism behind the differences between Figs. 3 and 4. Since the orbital period of a separatrix is infinite, the conservation of the integral (33) is no longer guaranteed, and, indeed, the adiabatic invariant could have a jump at a separatrix crossing (Murray & Dermott 2000). Still, we can estimate the post-crossing adiabatic invariant, using the continuity of the trajectory.

Now we concretely discuss the separatrix crossings for patterns P1, P2 and P3 shown in Fig. 8. For the pattern P1, let us consider a trajectory in a retrograde circulation (above the red separatrix) in Fig. 8b, with its adiabatic invariant S_0 . The separatrix crossing occurs when the area of the librating region (inside the red separatrix) increases to S_0 . After the crossing, the trajectory smoothly become a librating trajectory around the fixed point at $g_1 = \pi/2$. Due to the continuity, its adiabatic invariant is same as the original value S_0 .

Next, for the pattern P3 in Fig. 8d, we examine a librating trajectory above the blue separatrix, with its adiabatic invariant S'_0 (the area inside the trajectory around the stable fixed point at $g_1 = \pi/2$). When the area of the whole

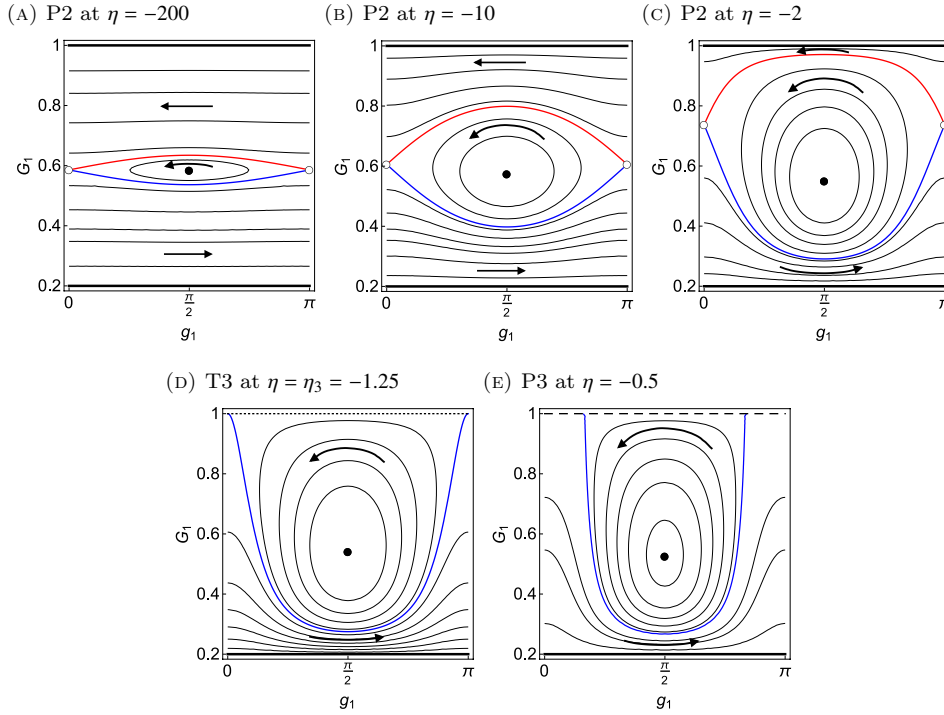


Figure 9. Evolution of the phase space for $(J_1, p) = (0.2, 0.2)$ (in the region III) that has only one transition T3 at $\eta_3 = -1.25$. The patterns P2 and P3 are separated by the transition T3. For P2, the libration region is between the red and blue separatrices and its area asymptotically approaches to 0 in the limit $\eta \rightarrow -\infty$.

librating region bounded by the blue separatrix decreases down to S'_2 , the trajectory crosses the separatrix and starts prograde circulation. At the crossing, the adiabatic invariant has a gap and becomes

$$(1 - J_1)\pi - S'_2. \quad (34)$$

Here, $(1 - J_1)\pi$ is the total area of the phase space.

As discussed above, the separatrix crossing for the two patterns P1 and P3 (and also P4) can be easily understood. Therefore, hereafter, we concentrate on the crossing for the pattern P2 that has two separatrices and three distinct regions, as in Figs. 9a-9c.

To begin with, we define the following two integrals

$$S_+(\eta) = \int_0^\pi (\tilde{G}_{1,+}(\eta) - J_1) dg_1, \quad (35)$$

$$S_-(\eta) = \int_0^\pi (\tilde{G}_{1,-}(\eta) - J_1) dg_1. \quad (36)$$

respectively corresponding to the areas below the upper (red) and lower (blue) separatrices of the pattern P2.

As an example of a separatrix crossing for the pattern P2, in Fig. 9a, we consider a retrogradely circulating trajectory above the red separatrix with its adiabatic invariant S''_0 . As η increases, the area $S_+(\eta)$ grows and the separatrix crossing occurs at $\eta = \eta_c$ where we have

$$S''_0 = S_+(\eta_c). \quad (37)$$

After the crossing, the trajectory shifts to either of the following two trajectories. One is a librating motion inside the two separatrices and the adiabatic invariant becomes

$$S_+(\eta_c) - S_-(\eta_c). \quad (38)$$

The other is the circulating one below the blue separatrix, with the post-crossing value

$$S_-(\eta_c). \quad (39)$$

The branching ratio of these two will be discussed in §5.3.

5.2 Tracing the evolution of trajectories

In this subsection, we discuss the time evolution for the two runs, R3 and R4 already introduced in §3 (see also Figs. 3 and 4). These are given for the parameters $(J_1, p) = (0.2, 0.2)$, and the phase space has the single transition T3 at $\eta_3 = -1.25$ (see Table 2 and Fig. 7).

At the initial epoch $\eta = -20$, the two trajectories commonly have $G_1 = 0.95$ and $g_1 \sim 0$, and thus their adiabatic invariants are effectively the same 2.37. From this value and the condition (37), we can predict the epoch $\eta_c = -1.66$ for the separatrix crossing and can also evaluate the areas at that time

$$S_+(\eta_c) = 2.37, \quad S_-(\eta_c) = 0.68. \quad (40)$$

In Figs. 10 and 11, at $\eta = -20, -1.68, -1.64$ and -1.20 , we present the snapshots of the two runs R3 and R4 obtained by numerically integrating the canonical equations (as described in §3), along with the separatrices. The boundaries of the green regions are the contours of our Hamiltonian, determined analytically from the relevant adiabatic invariants. Here, we appropriately included the predicted changes at the separatrix crossings, as explained in §5.1. More specifically, in Fig. 10, the areas for the green regions are respectively, (a) $S_+(\eta_c) = 2.37$, (b) 2.37, (c) $S_-(\eta_c) = 0.68$ and (d) 0.68.

Meanwhile, in Fig. 11, the areas are (a) 2.37, (b) 2.37, (c) $S_+(\eta_c) - S_-(\eta_c) = 1.69$ and (d) $(1 - J_1)\pi - 1.69 = 0.82$.

From the good agreements between the numerical results (cyan points) and the predictions (the boundaries of the green regions), we can confirm the usefulness of the adiabatic invariant and its transitions at separatrix crossings.

In Figs. 10 and 11, the two trajectories have almost the same evolution before the separatrix crossing around the predicted value $\eta_c = -1.66$. After the crossing, the two trajectories show distinct bifurcation. As shown in Fig. 10, the trajectory of the run R3 starts a prograde circulation below the blue separatrix, and its eccentricity $e_1 = \sqrt{1 - G_1^2}$ suddenly increases, consistent with Fig. 3. Its later evolution is well predicted by the new adiabatic invariant 0.68 with no additional separatrix crossing.

On the other hand, in Fig. 11c, after $\eta = \eta_c$, the trajectory of the run R4 has a librating motion between the two separatrices, and the range of its eccentricity oscillation becomes larger, including the original range (as observed in Fig. 4). This trajectory has the secondary separatrix crossing at $\eta = -1.22$, and temporarily takes $G_1 \approx 1$, corresponding to $e_1 \approx 0$ (also seen in Fig. 4). In this manner, we can understand the notable differences between Figs. 3 and 4, though the structure of the separatrices.

5.3 Probability of bifurcation

As discussed so far, the phase-space pattern P2 has the two circulating regions and the intermediate librating region. In Figs. 10 and 11, when an upper circulating trajectory crosses the red separatrix, it could either move to the lower circulating region or the librating region, depending sensitively on the initial conditions. Even though the canonical equations (22) are purely deterministic, we can effectively regard this bifurcation process as probabilistic, given the strong dependence of the initial conditions.

In this subsection, concentrating on the pattern P2, we discuss the branching ratio specifically for the upper circulating trajectory at the separatrix crossings (see Henrard 1982; Borderies & Goldreich 1984; Murray & Dermott 2000; Binney & Tremaine 2008 for related analysis on mean motion resonances). We can easily extend our arguments for the separatrix crossings from other two regions (as briefly mentioned at the end of this subsection).

We consider the time evolution of the phase space associated with given parameters (J_1, p) . To begin with, we define the following two quantities

$$v_+(\eta) \equiv \frac{dS_+(\eta)}{d\eta}, \quad v_-(\eta) \equiv \frac{dS_-(\eta)}{d\eta}, \quad (41)$$

representing the variation rates of the areas below the two separatrices. Additionally, we define $P_L(\eta)$ as the transition probability of an upper circulating trajectory into the librating region, just crossing the upper separatrix at the epoch η . This definition should be correctly kept in mind, for the arguments below. Our goal in this subsection is provide the simple expression for $P_L(\eta)$.

Actually, for our system, we generally have $v_+(\eta) > 0$ for the pattern P2 with $v_+(\eta_3) = 0$ at the transition T3. During the time interval between η and $\eta + \Delta\eta$, the area $v_+(\eta)\Delta\eta > 0$ newly crosses the upper separatrix downwardly. The key

issue here is how this eroded upper phase-space element is redistributed to the lower circulating or the intermediate librating regions. Considering the Liouville's theorem, the probability $P_L(\eta)$ is given by the fraction of the original area $v_+(\eta)\Delta\eta$ redistributed to the intermediate librating region. For our system with $v_+ > 0$, depending on v_- , we have the following three cases C1-C3 (see Problem 3.43 in Binney & Tremaine 2008).

(C1) $v_+(\eta) \geq 0 \geq v_-(\eta)$. The area of the intermediate librating region increases by $(v_+ - v_-)\Delta\eta > 0$, but the lower circulating region decreases by $v_- \Delta\eta < 0$. Therefore, the upper circulating trajectory will be always absorbed into the librating region, and we identically have $P_L = 1$.

(C2) $v_+(\eta) \geq v_-(\eta) \geq 0$. The area of the lower circulating region increases by $v_- \Delta\eta > 0$ and, at the same time, that of the middle librating region increases by $(v_+ - v_-)\Delta\eta > 0$. Both increments are compensated by the decrement of the upper circulating region. Therefore, the transition probability is given as

$$P_L(\eta) = \frac{v_+(\eta) - v_-(\eta)}{v_+(\eta)} = 1 - \frac{v_-(\eta)}{v_+(\eta)}. \quad (42)$$

(C3) $v_-(\eta) \geq v_+(\eta) \geq 0$. Only the lower circulating region increases, and thus it always absorbs the upper circulating trajectory, resulting in $P_L = 0$.

In order to clarify the boundaries between these three cases, we define the two epochs η_{eq} and η_z with the following conditions

$$v_+(\eta_{\text{eq}}) = v_-(\eta_{\text{eq}}), \quad v_-(\eta_z) = 0. \quad (43)$$

The boundary between C2 and C3 is at $\eta = \eta_{\text{eq}}$, and that between C1 and C3 is at $\eta = \eta_z$.

In the next subsection, we concretely evaluate the probability P_L as a function of the initial eccentricity $e_{1,i}$ given at a large negative $\eta (\ll -1)$. For $\eta \ll -1$, the g_1 dependence can be ignored for our Hamiltonian (7), and thus its contour line is nearly parallel to the g_1 -axis (see Fig. 8a). This allows us to simply evaluate the initial adiabatic invariant S_i as follows

$$S_i(e_{1,i}) \equiv \pi \left(\sqrt{1 - e_{1,i}^2} - J_1 \right). \quad (44)$$

Then, we can relate the epoch of the separatrix crossing η_c with the initial eccentricity $e_{1,i}$, using the following equation

$$S_i(e_{1,i}) = S_+(\eta_c). \quad (45)$$

We formally express their relation by $e_{1,i}(\eta_c)$ and $\eta_c(e_{1,i})$. For example, as a function of the initial eccentricity $e_{1,i}$, the transition probability is simply given by

$$P_L[\eta_c(e_{1,i})]. \quad (46)$$

Here, it should be noted that, with the identity $v_+ > 0$ in the phase P2, the probabilistic bifurcation corresponding to C2 can be realized only for the separatrix crossing from the upper circulating region. This is because the trajectories in the lower circulating region and the middle librating region cannot move into the upper circulating region and are not probabilistic.

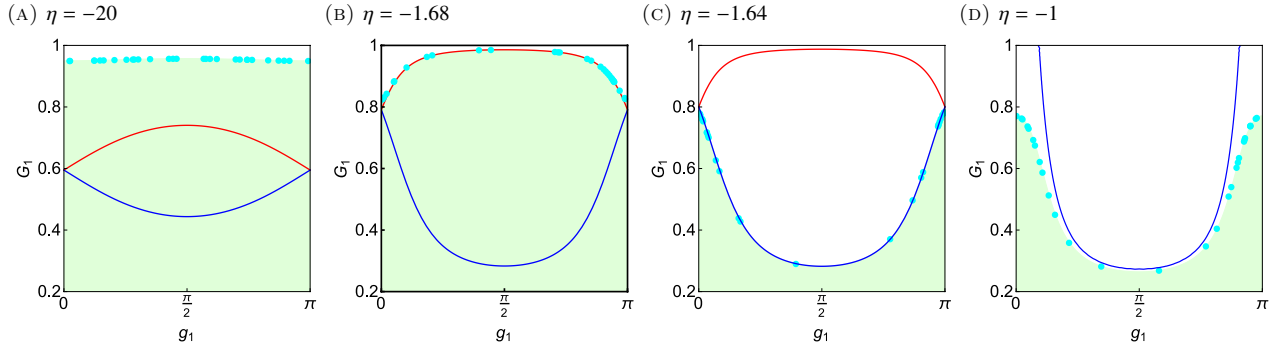


Figure 10. Evolution of a trajectory from the initial condition $(G_1, g_1) = (0.950, 0.04)$ at $\eta = -20$ with $(J_1, p) = (0.2, 0.2)$. The cyan points represent results obtained from the numerical runs R3 (also shown in Fig.3), and the areas of the green regions show the corresponding adiabatic invariants. The red and blue lines are the upper and lower separatrices $\tilde{G}_{1,+}$ and $\tilde{G}_{1,-}$. After the encounter with the red separatrix $\tilde{G}_{1,+}$ at $\eta \simeq -1.66$, the trajectory moved to the lower circulating region under the blue separatrix $\tilde{G}_{1,-}$. The green regions of (a) and (b) have the identical area. The same is true for (c) and (d).

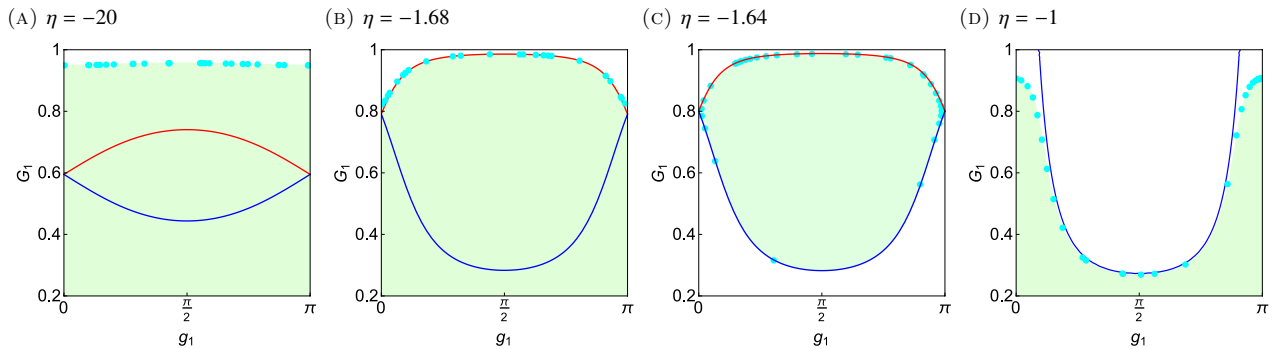


Figure 11. Same as Fig. 10, but from the initial conditions are $(G_1, g_1) = (0.950, 0.01)$. The cyan points are results from the run R4 (also shown in Fig.4). The trajectory is temporarily captured into libration region after the first separatrix crossing at $\eta \simeq -1.66$. Subsequently, it moves to the lower circulating region, crossing the blue separatrix at $\eta \simeq -1.22$. The green regions of (a) and (b) have the identical area. But (c) and (d) have different areas.

5.4 Application of the probability formula to our systems

Now, we provide some examples for the bifurcation probability $P_L(e_{1,i})$ as a function of the initial eccentricity $e_{1,i}$ defined at $\eta \ll -1$. We should recall that, in §5.3 and 5.4, we deal with the separatrix crossing and associated bifurcation only for the pattern P2.

The pattern P2 is realized for the parameters (J_1, p) in the regions I-IV in Fig. 7. As mentioned earlier, in these regions, we always have $v_+ > 0$ for P2 with $v_+(\eta_3) = 0$ at the final epoch $\eta = \eta_3$ (the transition T3). Since the upper separatrix converges to $G_1 = 1$ at $\eta = \eta_3$, we also have the corresponding eccentricity $\lim_{\eta \rightarrow \eta_3} e_{1,i}(\eta) = 0$.

Below, we analyze the three representative models with $(J_1, p) = (0.2, 0.8), (0.2, 0.2)$ and $(0.1, 0.9)$. Their basic parameters are summarized in Fig. 4.

5.4.1 $(J_1, p) = (0.2, 0.8)$ in the region II

In Fig. 12, we provide the rates v_+ and v_- for $(J_1, p) = (0.2, 0.8)$ that has the pattern P2 during the finite interval $-1.64 < \eta < -1.25$ (see Table 4). During this interval, the trajectory-

Table 4. The transitions realized for our three examples of (J_1, p) . The important transition epochs η and the associated eccentricities $e_{1,i}(\eta)$ (through Eq. (45)) are presented. The eccentricities with asterisk are given by Eq. (48) for $\eta = -\infty$.

(J_1, p)	η_2	η_z	η_{eq}	η_3
	$e_{1,i}(\eta_2)$	$e_{1,i}(\eta_z)$	$e_{1,i}(\eta_{\text{eq}})$	$e_{1,i}(\eta_3)$
(0.8, 0.2)	-1.64	-	-1.35	-1.25
	0.39	-	0.17	0
(0.2, 0.2)	-	-2.07	-1.37	-1.25
	0.81*	0.40	0.15	0
(0.1, 0.9)	-	-	-	-10
	0.26*	-	-	0

ries with initial eccentricities $0 < e_{1,i} < 0.39$ cross the upper separatrix downwardly. In Fig. 12, we have the transition epoch $\eta_{\text{eq}} = -1.35$ with $e_{1,i}(\eta_{\text{eq}}) = 0.17$. Then, as discussed in the previous subsection and shown in Fig. 13, we have

$$P_L(e_{1,i}) = \begin{cases} \text{Eq.(42)} & (0.17 < e_{1,i} < 0.39) \\ 0 & (0 < e_{1,i} \leq 0.17). \end{cases} \quad (47)$$

Every point in the regions II and IV in Fig. 7 has a bifurcation probability $P_L(e_{1,i})$ whose profile is similar to Fig. 13.

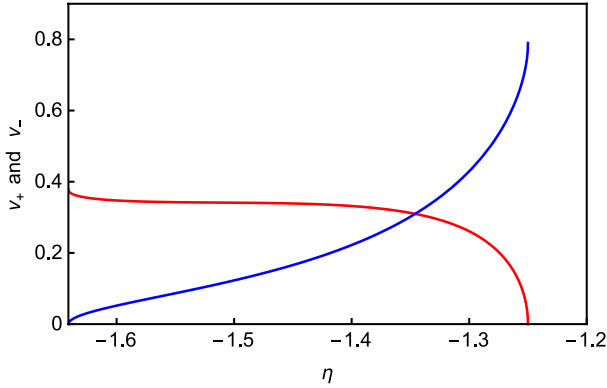


Figure 12. The rates $v_+(\eta)$ (red line) and $v_-(\eta)$ (blue line) for $(J_1, p)=(0.8, 0.2)$ in the region II (see Fig.7).

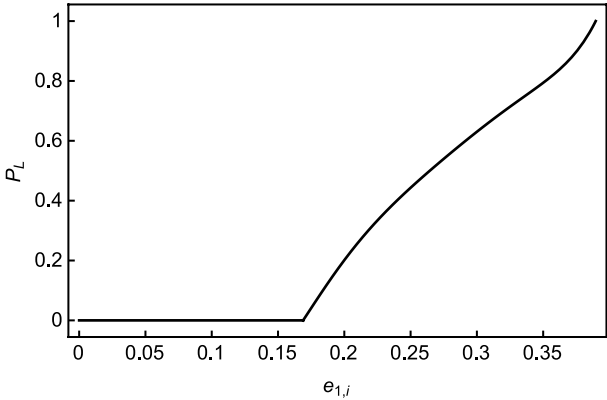


Figure 13. The transition probability P_L into libration for $(J_1, p)=(0.8, 0.2)$. The horizontal axis represents the inner eccentricity $e_{1,i}$ at $\eta \ll -1$.

5.4.2 $(J_1, p) = (0.2, 0.2)$ in the region III

Meanwhile, in the regions I and III in Fig. 7, the pattern P2 is realized for $\eta < \eta_3$ without a lower bound, and we have $\lim_{\eta \rightarrow -\infty} \bar{G}_{1,+}(g_1, \eta) = p^{1/3}$ for the upper separatrix (see §4.2). This asymptotic value corresponds to the initial eccentricity $e_{1,i} = \sqrt{1 - p^{2/3}}$,

$$(48)$$

and is provided in Table 4 with the asterisk *.

In Fig. 14, for $(J_1, p) = (0.2, 0.2)$, we show the rates v_+ and v_- at $\eta < \eta_3$. Now, Eq. (48) is given as $e_{1,i} = 0.81$, and the trajectories with initial eccentricity $0 < e_{1,i} < 0.81$ cross the upper separatrix, during $\eta < \eta_3 = -1.25$ (see Table 4).

In Fig. 15, we provide the probability $P_L(e_{1,i})$ for these eccentricities. With respect to the cases C1, C2 and C3 explained in the previous subsection, we have the two critical epochs $\eta_z = -2.07$ and $\eta_{eq} = -1.37$, corresponding to $e_{1,i} = 0.40$ and 0.15 respectively. Therefore, as shown in Fig. 15, we have

$$P_L(e_{1,i}) = \begin{cases} 1 & (0.40 \leq e_{1,i} < 0.81) \\ \text{Eq.(42)} & (0.15 < e_{1,i} < 0.40) \\ 0 & (0 < e_{1,i} \leq 0.15). \end{cases} \quad (49)$$

We also mention that the area of the lower circulating region in the pattern P2 (see Fig. 9) becomes minimum at

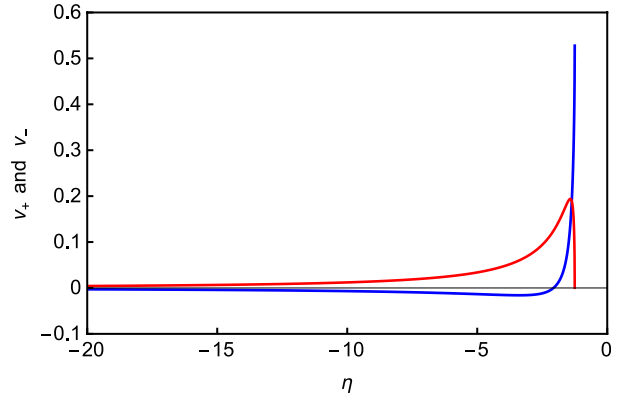


Figure 14. Similar to Fig. 12 but for $(J_1, p)=(0.2, 0.2)$. The red line is for $v_+(\eta)$ and the blue line is for $v_-(\eta)$.

$\eta_z = -2.07$. This area corresponds to the initial eccentricity $e_{1,i} = 0.91$.

For the parameters $(J_1, p) = (0.2, 0.2)$, the characteristic initial eccentricities $e_{1,i} = 0.15, 0.40, 0.81$ and 0.91 play important roles later in §5.5.

5.4.3 $(J_1, p) = (0.1, 0.9)$ in the region III

For $(J_1, p) = (0.1, 0.9)$, in contrast to $(0.2, 0.2)$, we identically have $v_- < 0$ for $\eta < \eta_3$, as shown in Fig. 16. Therefore, the bifurcation probability becomes $P_L(e_{1,i}) = 1$ throughout $\eta < \eta_3$.

Actually, for the parameters (J_1, p) in the regions I and III, the characteristic profiles of the rates (v_+, v_-) are either like Fig. 14 or Fig. 16. In fact, it was numerically confirmed that we have at most one solution η_{eq} for the equation $v_-(\eta_{eq}) = 0$.

Then, additionally considering the general profile of the function $v_+(\eta)$ (namely $v_+(\eta) > 0$ for $\eta < \eta_3$ and $v_+(\eta_3) = 0$), the existence of the probabilistic bifurcation C2 is determined only by the sign of $v_-(\eta_3)$. For $v_-(\eta_3) < 0$, we always have $P_L(e_{1,i}) = 1$ at $\eta < \eta_3$, as demonstrated for the example $(J_1, p) = (0.1, 0.9)$. But for $v_-(\eta_3) > 0$, we have the probabilistic bifurcation C2, as shown in Figs. 14 and 15 for $(J_1, p) = (0.2, 0.2)$. In the end, based on this criteria $v_-(\eta_3) < 0$, we numerically found that, in the regions I-IV shown in Fig. 7, only the shaded region does not contain the probabilistic bifurcation C2.

5.5 maximum eccentricity

As mentioned earlier, realization of a large eccentricity could result in astrophysically intriguing phenomenon such as tidal disruption events and gravitational wave bursts. In this subsection, for each trajectory, we examine its maximum eccentricity observed in a certain time interval.

For the two sets of model parameters $(J_1, p) = (0.2, 0.2)$ and $(0.15, 0.001)$, we basically follow the evolution of the whole trajectories in the phase space from $\eta = -20$ down to -0.7 , fixing the infall rate at $\dot{\eta} = 10^{-2}$.

At the initial epoch $\eta = -20$, we start the orbital evolution from $(g_1, G_1) = (\pi/2, \sqrt{1 - e_{1,ini}})$ with the input parameter $e_{1,ini}$.

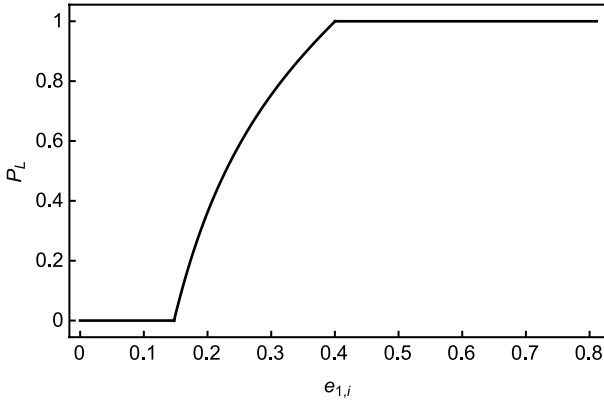


Figure 15. The transition probability into libration similar to Fig. 13 but for $(J_1, p) = (0.2, 0.2)$.

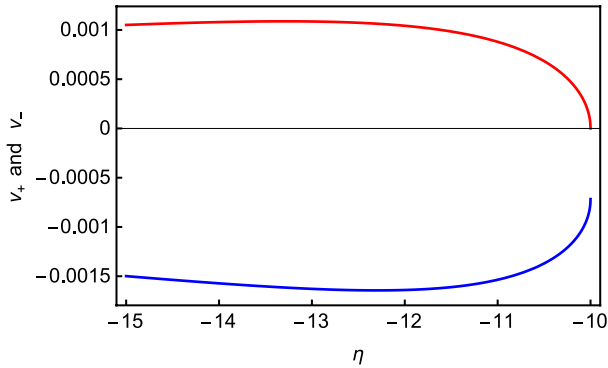


Figure 16. Similar to Fig. 12 but for $(J_1, p) = (0.1, 0.9)$. The red line is for $v_+(\eta)$ and the blue line is for $v_-(\eta)$. We identically have $v_-(\eta) < 0$ for the pattern P2, resulting in $P_L(\eta) = 1$.

For each trajectory, we read the maximum eccentricity $e_{1,\max}$ during the final rotation period at the termination epoch $\eta = -0.7$. Both of the two models have the phase-space pattern P3 (see *e.g.* Fig.8d) at $\eta = -0.7$, and the local maximum $e_{1,\max}$ is easily obtained from the G_1 -coordinate of the trajectory, when taking the phase $g_1 = \pi/2$ below the stable fixed point.

Here, we should notice that, using $e_{1,\text{ini}}$ and $e_{1,\max}$ respectively, we can uniquely specify the orbital contour in the phase spaces at the two epochs $\eta = -20$ and -0.7 (see *e.g.* Figs.8b and 8d). Meanwhile, for each trajectory, we also define $e_{1,\max,\text{his}}$ as the global maximum of the eccentricity e_1 recorded between $\eta = -20$ and -0.7 .

5.5.1 results for $(J_1, p) = (0.2, 0.2)$

In Figs. 17 and 18, we provide the correspondence between the initial eccentricity $e_{1,\text{ini}}$ and the final one $e_{1,\max}$ for $(J_1, p) = (0.2, 0.2)$. From $\eta = -20$ to -0.7 , the eccentricity of the stable fixed point (at $g_1 = \pi/2$) monotonically increases from $e_1 = 0.81$ to 0.85 (see Fig.9). Furthermore, for this model parameters, we simply have $e_{1,\max,\text{his}} = e_{1,\max}$, because of the evolutionary profile of the phase space. In Fig. 17, we have $e_{1,\max} \geq 0.85$, as easily understood from the definition of $e_{1,\max}$.

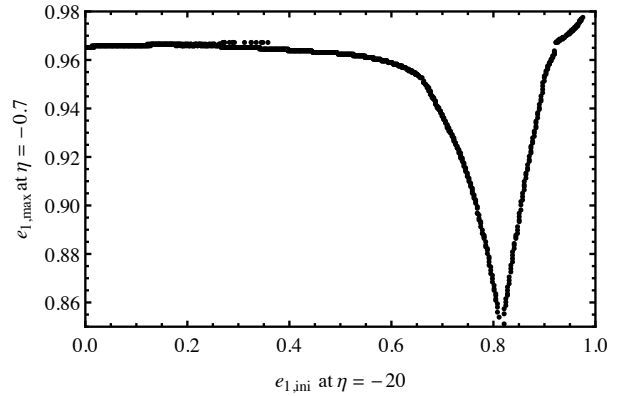


Figure 17. The correspondence between the initial eccentricity $e_{1,\text{ini}}$ at $\eta = -20$ and the final eccentricity $e_{1,\max}$ at $\eta = -0.7$. The initial phase of the trajectory is $g_1 = \pi/2$. The final eccentricity $e_{1,\max}$ is the local maximum that is realized during the final rotation cycle in our phase space. The model parameters are $(J_1, p) = (0.2, 0.2)$. For this model, the global maximum $e_{1,\max,\text{his}}$ is identical to the local one $e_{1,\max}$.

As discussed in §5.3, at $\eta = -\infty$, a trajectory in the phase space moves on a horizontal line characterized by the eccentricity $e_{1,i}$. At $\eta = -20$, a trajectory is no longer a straight line, but we still have $e_{1,\text{ini}} \simeq e_{1,i}$ for each trajectory. In fact, the characteristic eccentricities mentioned in §5.4.2 appears clearly in Fig. 18 where we define the end points A, B, D, E, F and the junction point C. More specifically, the points A and F have $e_{1,\text{ini}} \simeq e_{1,i} = 0.91$, while B and F have $e_{1,\text{ini}} \simeq e_{1,i} = 0.40$. At the critical epoch $\eta = \eta_c = -2.07$, these two eccentricities correspond to the circulating trajectories just below the lower separatrix and just above the upper separatrix, respectively (see Fig. 9).

In Fig. 18, the point C has $e_{1,\text{ini}} \simeq e_{1,i} = 0.15$, related to the upper separatrix at $\eta = \eta_c = -1.37$. The two branches BC and EC are the components of the probabilistic bifurcation discussed in §5.4.2. After $\eta > \eta_c$, the former moved below the lower separatrix. Meanwhile, the segment EC was captured into the middle libration regime, encircling the branch EF that had already entered the libration regime at $\eta = \eta_c$. Therefore, the vertical gaps AF and BE are the same.

Next, by studying the inverse mapping $e_{1,\max} \rightarrow e_{1,\text{ini}}$, we can see how the final phase-space is constituted by the initial phase-space elements. For example, the EF branch is a double value function of the final quantity $e_{1,\max}$. This part is originally caused by the blending of two distinct regions in the phase-space, along with the expansion of the middle circulating regime (see Figs. 9a and 9b).⁴

5.5.2 results for $(J_1, p) = (0.15, 0.001)$

In Figs. 19 and 20, we present the locally maximum value $e_{1,\max}$ (black points) at $\eta = -0.7$ and the globally maximum value $e_{1,\max,\text{his}}$ (green points) recorded between $\eta = -20$ and -0.7 . These are given for $(J_1, p) = (0.15, 0.001)$.

⁴ Strictly speaking, the range $0.85 < e_{1,\max} < 0.95$ is already inside the libration region at $\eta = -20$. The blending between $-20 < \eta < -0.7$ is only for the upper part $0.95 < e_{1,\max} < 0.964$.

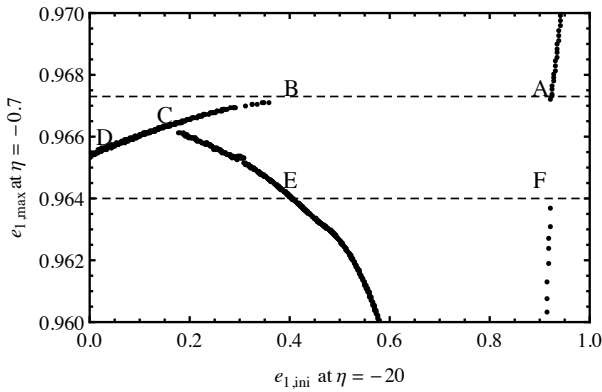


Figure 18. The detailed figure for Fig. 17 around $e_{1,\max} = 0.966$. We introduce the labels A,B,D,E and F for the end points, and C for the junction point.

For the simpler case $p = 0$, the phase space has the pattern P1 (see *e.g.* Fig. 8) in the period $\eta_1 < \eta < -1 (= \eta_2 = \eta_3)$. The red (upper) separatrix sweeps the whole phase space in this period. At the separatrix crossing, because of the profile of the upper (red) separatrix during P1, we have $G = J_1$, and all the trajectories temporarily take $e_1 = \sqrt{1 - J_1^2}$ which is the allowed maximum value. The main reason for adopting the present parameter $p = 0.001$ here is to examine how this simple result for $p = 0$ is modified for a small but finite p .

As demonstrated in Fig.19, we actually have

$$e_{1,\max,\text{his}} \simeq \sqrt{1 - J_1^2} = 0.9887 \quad (50)$$

for initial eccentricity $e_{1,\text{ini}} < 0.93$. This result clearly shows that the characteristic motion associated with a separatrix could be an efficient mechanism to realize a large eccentricity and promote the strong interaction between stars and the central black hole. In Fig. 19, we should notice that, at $\eta = -20$, trajectories with $e_{1,\text{ini}} > 0.93$ are already inside the libration zone around the stable fixed point, and could not preferably cross the separatrix during our calculation. We also have

$$e_{1,\max,\text{his}} > e_{1,\max}, \quad (51)$$

since the global maximum $e_{1,\max,\text{his}}$ is recorded at the separatrix crossing, in contrast to the previous example with $(J_1, p) = (0.2, 0.2)$.

In Fig. 20, we take a closer look at $e_{1,\max,\text{his}}$ around $\sqrt{1 - J_1^2} = 0.9887$. We can see a break at

$$e_{1,\text{ini}} \sim 0.57. \quad (52)$$

Actually, for $e_{1,\text{ini}} < 0.57$, the trajectory cross the upper separatrix during the pattern P2 (after $\eta = \eta_2 = -1.42$), not P1. But the lower (blue) separatrix during P2 does not pass the lowest end $G_1 = J_1$ of our phase-space⁵, resulting in

$$e_{1,\max,\text{his}} < \sqrt{1 - J_1^2}. \quad (53)$$

⁵ Fig. 8c is not clear-cut about this. See *e.g.* Fig 9c for a more illustrative example.

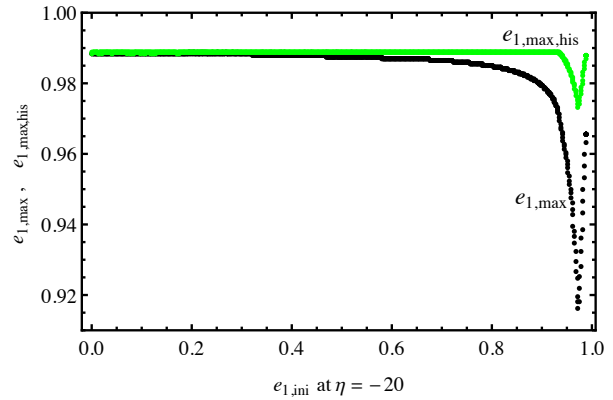


Figure 19. Similar to Fig. 19, but for the model parameters $(J_1, p) = (0.15, 0.001)$. The black points are for the local maximum $e_{1,\max}$ at $\eta = -0.7$, while the green points represent the global maximum $e_{1,\max,\text{his}}$ recorded between $\eta = -20$ and -0.7 . In contrast to Fig. 17, we now have $e_{1,\max,\text{his}} > e_{1,\max}$.

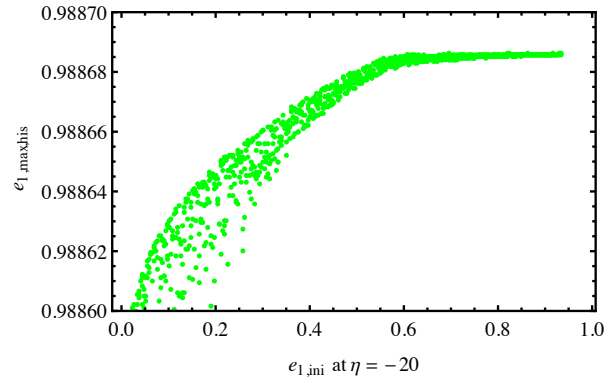


Figure 20. The detailed figure for Fig. 19 around $e_{1,\max} = \sqrt{1 - J_1^2} = 0.9887$. Only the global maximum $e_{1,\max,\text{his}}$ are shown. We have a break around $e_{1,\text{ini}} = 0.58$.

The scatter in Fig. 20 is mainly caused by the finiteness of $\dot{\eta}$, not by numerical errors. In fact, we confirmed that the scatter is decreased for a slower rate $\dot{\eta}$.

6 SUMMARY

Using the framework of the secular theory for a hierarchical triple system, we have studied the long-term orbital evolution of individual stars in a galactic nuclear star cluster to which an secondary MBH is gradually infalling with vanishing eccentricity. Our secular Hamiltonian $\mathcal{H}_T(g_1, G_1; \eta)$ is composed by the three terms; the quadrupole gravitational field \mathcal{H}_{qp} induced by the outer MBH, the gravitational potential \mathcal{H}_{SP} of the cluster itself, and the post-Newtonian correction \mathcal{H}_{IPN} due to the central MBH. This Hamiltonian has two constant parameters (J_1, p) and is described by the effective time variable η .

As demonstrated in Figs. 3 and 4, the eccentricities of stars in the cluster could show sharp transitions that depend strongly on their initial conditions. Our primary goal in this

paper was to understand the mechanism behind these interesting behaviors, through the phase-space evolution of our Hamiltonian induced by the infalling outer MBH.

To closely examine the phase-space evolution, we first analyzed distribution of fixed points and identified the five critical transitions at η_i ($i = 1, \dots, 5$) when their basic properties (*e.g.* number, stability) change (see Table 2). As shown in Fig. 7, the parameters (J_1, p) determine the combinations of the transitions that are realized during the infall of the secondary MBH. Then, we showed that, in the phase-space, the profile of the separatrices can be divided into the five types P0 to P4 (see Fig. 8). The particularly important one P2 is generated by a competition between the prograde apsidal precession enforced by the two terms \mathcal{H}_{qp} and \mathcal{H}_{IPN} and the retrograde one by the remaining term \mathcal{H}_{SP} .

Next, we traced the evolution of individual orbits in the time varying phase-space. Here, we applied a geometrical approach using the adiabatic invariant, and confirmed its validity. Taking a step further, we calculated the branching ratio of a bifurcation at a separatrix crossing that plays a crucial role for the notable behaviors in Figs. 3 and 4.

Our analytical studies have been somewhat abstract. But the characteristic behaviors (*e.g.* the sharp probabilistic bifurcations and the transient realizations of large eccentricities) would be identified in N-body simulations. These are the clear signatures of the separatrix crossings that are originally induced by the decay of the outer orbit. As mentioned earlier, in the numerical simulations in Bode & Wegg (2014), the outer orbit decays faster than the KL oscillations. Meanwhile, in Li et al. (2014), the outer orbit is fixed. Therefore, it is not surprising that the characteristic behaviors were not reported in these papers.

In the field of celestial mechanics, geometrical studies similar to this paper have long been made for mean-motion resonances, including probabilistic bifurcations at the resonant capture (Murray & Dermott 2000). We expect that our analysis for the secular theory would help us to develop a deep understanding of orbital dynamics related to separatrix crossing, from a wider perspective.

Our Hamiltonian is a one-dimensional system with the dynamical variables (g_1, G_1) . When the outer orbit is eccentric, the octupole term can enrich the system, involving the additional set of conjugate variables (Ω_1, J_1) for the inner orbit. Here Ω_1 is the longitude of ascending node. For example, it is well known that the octupole term can generate chaotic behaviors (Naoz 2016). Since a separatrix is also closely related to chaos, it would be interesting to study the effects of the outer eccentricity (for related processes, see Iwasawa et al. 2011; Sesana, Gualandris & Dotti 2011; Madigan & Levin 2012; Merritt 2013; Vasiliev, Antonini & Merritt 2015).

Our study is based on the secular theory that introduces the averaging operations for the inner and outer orbits. But this prescription is known to break down for highly eccentric inner orbits that would be especially important for astrophysical phenomenon, such as the tidal disruption events or gravitational wave emissions (Katz & Dong 2012; Bode & Wegg 2014). Direct N-body simulations would be useful to quantitatively examine the related issues and also evaluate the relaxation effects.

ACKNOWLEDGEMENTS

This work is supported by JSPS Kakenhi Grant-in-Aid for Scientific Research (No. 15K05075) and for Scientific Research on Innovative Areas (Nos. 24103006 and 17H06358).

REFERENCES

- Alexander T., 2005, *Phys.Rep.*, 419, 65
 Antognini J. M., Shappee B. J., Thompson T. A., Amaro-Seoane P., 2014, *MNRAS*, 439, 1079
 Antognini J. M. O., 2015, *MNRAS*, 452, 3610
 Antonini F., Murray N., Mikkola S., 2014, *ApJ*, 781, 45
 Antonini F., Perets H. B., 2012, *ApJ*, 757, 27
 Batygin K., 2015, *MNRAS*, 451, 2589
 Binney J., Tremaine S., 2008, *Galactic Dynamics: Second Edition*. Princeton University Press
 Blaes O., Lee M. H., Socrates A., 2002, *ApJ*, 578, 775
 Bode J. N., Wegg C., 2014, *MNRAS*, 438, 573
 Borderies N., Goldreich P., 1984, *Celestial Mechanics*, 32, 127
 Borkovits T., Hajdu T., Sztakovics J., Rappaport S., Levine A., Bíró I. B., Klagyivik P., 2016, *MNRAS*, 455, 4136
 Chen X., Sesana A., Madau P., Liu F. K., 2011, *ApJ*, 729, 13
 Eggleton P., Kiseleva L., 1995, *ApJ*, 455, 640
 Fabrycky D., Tremaine S., 2007, *ApJ*, 669, 1298
 Fabrycky D. C. et al., 2014, *ApJ*, 790, 146
 Ferrarese L., Ford H., 2005, *Space Science Reviews*, 116, 523
 Ford E. B., Kozinsky B., Rasio F. A., 2000, *ApJ*, 535, 385
 Goldreich P., 1965, *MNRAS*, 130, 159
 Goldreich P., Schlichting H. E., 2014, *AJ*, 147, 32
 Hamers A. S., Lai D., 2017, *ArXiv e-prints*
 Hamers A. S., Portegies Zwart S. F., 2016, *MNRAS*, 459, 2827
 Harrington R. S., 1968, *AJ*, 73, 190
 Henrard J., 1982, *Celestial Mechanics*, 27, 3
 Henrard J., Lamaitre A., 1983, *Celestial Mechanics*, 30, 197
 Hoffman L., Loeb A., 2007, *MNRAS*, 377, 957
 Holman M., Touma J., Tremaine S., 1997, *Nature*, 386, 254
 Ivanov P. B., Polnarev A. G., Saha P., 2005, *MNRAS*, 358, 1361
 Iwasa M., Seto N., 2016, *Phys. Rev. D*, 93, 124024
 Iwasawa M., An S., Matsubayashi T., Funato Y., Makino J., 2011, *ApJ*, 731, L9
 Katz B., Dong S., 2012, *ArXiv e-prints*
 Kinoshita H., Nakai H., 1999, *Celestial Mechanics and Dynamical Astronomy*, 75, 125
 Kocsis B., Tremaine S., 2011, *MNRAS*, 412, 187
 Kozai Y., 1962, *AJ*, 67, 591
 Kushnir D., Katz B., Dong S., Livne E., Fernández R., 2013, *ApJ*, 778, L37
 Landau L. D., Lifshitz E. M., 1969, *Mechanics*. Pergamon Press
 Li G., Naoz S., Holman M., Loeb A., 2014, *ApJ*, 791, 86
 Lidov M. L., 1962, *Planetary and Space Science*, 9, 719
 Lithwick Y., Wu Y., 2012, *ApJ*, 756, L11
 Luo L., Katz B., Dong S., 2016, *MNRAS*, 458, 3060
 Madigan A.-M., Levin Y., 2012, *ApJ*, 754, 42

Mardling R. A., Aarseth S. J., 2001, MNRAS, 321, 398
 McConnell N. J., Ma C.-P., 2013, ApJ, 764, 184
 Merritt D., 2013, Dynamics and Evolution of Galactic Nuclei. Princeton University Press
 Michaely E., Perets H. B., 2014, ApJ, 794, 122
 Muñoz D. J., Lai D., Liu B., 2016, MNRAS, 460, 1086
 Murray C. D., Dermott S. F., 2000, Solar System Dynamics. Cambridge University Press
 Nagasawa M., Ida S., Bessho T., 2008, ApJ, 678, 498
 Naoz S., 2016, ARA&A, 54, 441
 Naoz S., Fabrycky D. C., 2014, ApJ, 793, 137
 Naoz S., Farr W. M., Lithwick Y., Rasio F. A., Teyssandier J., 2011, Nature, 473, 187
 Peale S. J., 1987, Orbital resonances, unusual configurations and exotic rotation states among planetary satellites. Tech. rep.
 Pejcha O., Antognini J. M., Shappee B. J., Thompson T. A., 2013, MNRAS, 435, 943
 Perets H. B., Fabrycky D. C., 2009, ApJ, 697, 1048
 Rauch K. P., Tremaine S., 1996, New Astron, 1, 149
 Sesana A., Gualandris A., Dotti M., 2011, MNRAS, 415, L35
 Seto N., 2013, PRL, 111, 061106
 Shappee B. J., Thompson T. A., 2013, ApJ, 766, 64
 Silsbee K., Tremaine S., 2017, ApJ, 836, 39
 Sinclair A. T., 1972, MNRAS, 160, 169
 Stephan A. P., Naoz S., Ghez A. M., Witzel G., Sitarski B. N., Do T., Kocsis B., 2016, MNRAS, 460, 3494
 Strogatz S. H., 2014, Nonlinear Dynamics and Chaos: With Applications to Physics, Biology, Chemistry, and Engineering : Second Edition. Westview Press
 Thompson T. A., 2011, ApJ, 741, 82
 Toonen S., Hamers A., Portegies Zwart S., 2016, Computational Astrophysics and Cosmology, 3, 6
 Vasiliev E., Antonini F., Merritt D., 2015, ApJ, 810, 49
 Wegg C., Bode J., 2011, ApJ, 738, L8
 Wen L., 2003, ApJ, 598, 419
 Yoder C. F., 1973, PhD thesis, University of California, Santa Barbara.

profile had changed with time, the stars initially at a semi-major axis $x < a_c$ could keep isotropic density and velocity profile, because of the Liouville's theorem. In other words, the number density of stars in our phase-space (g_1, G_1) were initially homogeneous for an isotropic velocity profile, and the density of these stars has not changed with time both in the phase space and the positional space.

Meanwhile, the stars initially at a semimajor axis $x > a_c$ would now have anisotropic density profile that is axisymmetrical and also plane symmetric with respect to the outer orbital plane. For simplicity, we ignored the scatterings of semimajor axis from $x > a_c$ to $x < a_c$.

Given the inclination dependence of the orbital stability (*e.g.* Eggleton & Kiseleva 1995), the stellar density toward the equatorial direction ($I = \pi/2$) would be different from that of the polar directions ($I = 0$ and π). For an inner orbit at $x \ll a_c$, the gravitational effect of the outer anisotropic density profile at x would be approximately given by a positive or negative mass ring on the equator at x . Similar to the quadrupole effect of the outer MBH, contributions of these rings at $x > a_c$ would be effectively absorbed into the parameter η defined in Eq. (12) for our normalized Hamiltonian \mathcal{H}_r . Therefore, our Hamiltonian (7) would work better than natively expected. But, in any cases, detailed numerical simulations would be helpful to check validity of discussions in this appendix.

APPENDIX A: CLUSTER POTENTIAL

The stellar potential term \mathcal{H}_{sp} in Eq. (9) is derived under the assumptions that the nuclear stellar cluster is stationary and has isotropic density and velocity distributions up to infinite distance $r = \infty$. However, along with the contraction of the tertiary MBH m_2 from the outer part of the cluster, these assumptions are violated, *e.g.* due to orbital instabilities. Consequently, the stellar density (and thus potential) profile could become non-stationary and anisotropic. In this appendix, we briefly discuss how this outer boundary condition affects our Hamiltonian analysis for the inner orbital evolution.

For the stellar cluster, we define a_c as the semimajor axis above which the isotropies are violated. This length scale would be roughly proportional to a_2 the distance to the tertiary MBH, and decrease with time. Below, without loss of generality, we consider the situation (more specifically the potential term \mathcal{H}_{sp}) at a specific outer distance a_2 , and thereby fix the characteristic semimajor axis a_c .

First, we should notice that, even if the outer density